Striatin 3 and MAP4K4 cooperate towards oncogenic growth and tissue invasion in medulloblastoma

Jessica Migliavacca[1], Buket Züllig[1], Charles Capdeville[1], Michael Grotzer[2] and Martin Baumgartner[1,*]

[1] Division of Oncology, Children's Research Center, University Children's Hospital Zürich, Zürich, Switzerland

[2] Division of Oncology, University Children's Hospital Zürich, Zürich, Switzerland

*e-mail: Martin.Baumgartner@kispi.uzh.ch

The authors declare that they have no conflict of interest."

Abstract

MAP4K4 has been correlated with increased cell motility and reduced proliferation in mammalian cells. Consequences and regulation of this dichotomous functionality of MAP4K4 in tumor cells remained elusive. We find that MAP4K4 interacts with the STRN3 protein in medulloblastoma and that STRN3 and MAP4K4 exert opposing functions in Hippo tumor suppressor signaling and clonal growth. However, depletion of either STRN3 or MAP4K4 reduces migration and tissue invasion, and concomitant loss of both proteins halts tumor cell growth in the cerebellar tissue. Mechanistically, STRN3 couples MAP4K4 to the protein phosphatase 2A, which inactivates growth repressing activities of MAP4K4. In parallel, STRN3 enables growth factor-induced PKCθ activation and the direct phosphorylation of $VASP_{S157}$ by MAP4K4, which are necessary for efficient migration and tissue invasion. Thus, STRN3 controls MAP4K4 functionality in growth factor-activated tumor cells, and the cooperation of the two proteins promotes invasiveness through nPKCs and VASP and increases proliferation via inactivation of Hippo signaling. Targeting of the STRN3-MAP4K4 cooperation could reactivate Hippo signaling and repress invasiveness in growth factor-driven tumors.

Introduction

Medulloblastoma (MB) is the most common malignant brain tumor in children[1]. Four distinct molecular subgroups (Wingless (WNT), Sonic Hedgehog (SHH), group 3, and group 4) can be discriminated with a total of 12 subtypes[2–4]. The characteristic tendency of MB cells to locally infiltrate the cerebrospinal fluid (CSF) via leptomeningeal dissemination reduces the efficacy of current treatments[5]. One key driver of tissue invasion and growth in MB is the Fibroblast Growth Factor Receptor (FGFR) signaling pathway[6,7]. The molecular mechanisms that balance FGFR-driven tissue infiltration and growth in MB and other tumors remain incompletely understood, and no specific therapy is available to subvert this balance towards tumor suppression[8]. Tissue infiltration and growth rely on the complex orchestration of parallel, potentially opposing signaling pathways to overcome the incompatible concomitant induction of cell migration and growth. Improved anti-dissemination therapies should specifically repress both the pro-migratory and the proliferation promoting signaling in tumor cells. In this study we address the concomitant regulation of proliferation and invasiveness downstream of the activated FGFR, and we delineate the underlying molecular mechanisms and identify novel drug targets in MB.

The serine/threonine mitogen-activated protein kinase kinase kinase kinase 4 (MAP4K4/HGK/NIK), is upregulated in MB patient samples and acts as a critical promoter of receptor tyrosine kinase (RTK)-induced MB cell dissemination[9,10]. MAP4K4 controls a wide range of biological processes[11–16], which can be explained by the interaction of MAP4K4 with a number of structurally and functionally different effectors. The pro-migratory function of MAP4K4 is in part due to its capability to directly phosphorylate the ezrin, radixin, moesin (ERM) proteins, which mediate lamellipodium formation in response to growth-factor (GF) stimulation[17]. MAP4K4 couples GF signaling to actin polymerization through phosphorylation of the actin-related protein 2 (Arp2) subunit of the Arp2/3 complex, which increases its actin nucleation activity and triggers membrane protrusion in response to EGF[18]. In MB, MAP4K4 promotes turnover and activation of the receptor tyrosine kinase c-MET and of the β-1 integrin adhesion receptor, which is necessary for membrane protrusion at the leading edge of invading cells[10]. The pleiotropic functionality of MAP4K4 and its high expression in the healthy brain tissue argue against global pharmacological repression of its catalytic activity. Rather, more subtle interference strategies that target only subsets of its functions would be needed to repress MAP4K4 oncogenic activities specifically.

The related kinase Misshapen-like kinase (MINK)[19] and MAP4K4[20,21] were identified as components of the Striatin-interacting phosphatase and kinase (STRIPAK) complex[22–24]. The STRIPAK complex is a supramolecular scaffold assembled around the striatin family proteins (STRN, STRN3, STRN4). STRNs act as regulatory subunits of the protein phosphatase PP2A and are associated with STRN-interacting proteins (STRIP1/2) and with members of the germinal center kinase (GCK) families [22,25]. The STRIPAK complex controls Hippo tumor suppressor signaling towards YAP/TAZ transcriptional activation and proliferation by repressing associated Hippo-activating kinases including MAP4K4. In this context, STRIPAK-MAP4K4 interaction contributes to small T antigen-mediated cell transformation[21]. MAP4K4 interacts with STRN4, which on the one hand orchestrates MAP4K4 repression and thereby causes decreased Hippo signaling[20]. On the other hand, STRN4 was also proposed to repress malignant characteristics of cancer cells by blocking MAP4K4 functions. However, the mechanistic details how STRIPAK-controlled MAP4K4 contributes to tumorigenesis, in particular migration and tissue invasion, remain unresolved[26].

Using proximity-dependent biotin identification (BioID), we identified MAP4K4 as a component of the STRIPAK complex in MB cells. We explored whether MAP4K4-STRIPAK complex components are implicated in FGFR-driven cell dissemination, tissue invasion and growth in MB, and we identified underlying changes in relevant signaling pathways by kinase activity profiling. Our study identified the MAP4K4-STRIPAK complex as a central hub and bifurcation point, which promotes tissue invasion and growth in MB tumors. It provides relevant mechanistic insights in the regulation of these central processes in MB tumor cells, and it runs against the recently established dogma of STRIPAK-MAP4K4 antagonism by demonstrating a cooperative activity of STRN3 and MAP4K4 towards increased invasiveness.

Results

MAP4K4 is a component of the STRIPAK complex in MB cells

We used BioID to assess the MAP4K4 interactome and identified proteins biotinylated by FLAG-tagged N- or C-terminally biotin ligase-fused (BioID2[27]) full-length MAP4K4 (BioID2-MAP4K4 and MAP4K4-BioID2) or BioID2-FLAG alone through mass spectrometry (MS)[28,29] in HEK-293T cells (Figure S1A). The expression of 3xFLAG-tagged MAP4K4-BioID2 was confirmed by anti-FLAG immunoblot (IB) analysis and of biotinylation activity by horseradish peroxidase (HRP)-coupled

85 streptavidin binding (Figure S1B). Biotinylated proteins were enriched by affinity-capturing using
86 streptavidin-conjugated beads and subjected to MS. We identified a total of 156 MAP4K4-specific
87 proteins (Figure S1C, Table S1). Gene ontology (GO) analysis with these proteins predicted functions
88 such as endosomal transport[10], actin polymerization[18], or regulation of cell adhesion[16] (Figure
89 1A), and found enrichment of components of the STRIPAK complex (Figure 1A-C). We confirmed the
90 interaction of 3xFLAG-BioID2-MAP4K4 with STRN3, STRN4, and STRIP1 in HEK-293T cells by co-
91 immunoprecipitation analysis (Figure 1D). In agreement with other studies[30], these data confirm
92 MAP4K4 association with the STRIPAK complex in cells, possibly through direct interaction with STRN4
93 and STRN3.

94 We generated MB cell lines stably expressing either the 3XFLAG-BioID2-MAP4K4 fusion proteins or
95 BioID2 alone to test MAP4K4-STRIPAK complex interaction in these cells (Figure S1D). BioID2-
96 MAP4K4 localized to the cytoplasm, the primary residency of MAP4K4, where it co-localized with
97 biotinylated proteins (Figure S1E). In contrast, BioID2 distributes throughout the cells, with enrichment
98 in the nucleus. Streptavidin affinity purification-MS and anti-FLAG immunoprecipitation confirmed the
99 association of MAP4K4 with the STRIPAK complex in MB cells (Figure 1E,F, Figure S1F, Table S2).
100 MAP4K4 is dispensable for STRNs interaction with STRIP1, while STRN3 is necessary for MAP4K4
101 association with the complex (Figure 1G). Unlike other germinal center kinases that have been reported
102 to interact with STRIP1 in an activity-dependent manner[31], inhibition of MAP4K4 by GNE-495 did not
103 impact its constitutive association with STRN4, STRN3, and STRIP1 (Figure S1G). We generated DAOY
104 cells stably expressing 3XFLAG-tagged single domains or truncated versions of MAP4K4 (Figure 1H).
105 We found that N-terminally truncated MAP4K4 (ID1-ID2-CNH, 290-1273) pulled down STRN4 and
106 STRIP1 more effectively than C-terminally truncated KD-ID1-ID2 (1-954) (Figure 1H,I). The kinase
107 domain (KD, 1-289) or the intermediate domains (ID1, 290-634 or ID2, 635-954) alone are not sufficient
108 for pulling down STRN4 or STRIP1. Combined, these results suggest that the citron homology domain
109 (CNH, 954-1273) is required for MAP4K4-STRIPAK interaction.

110 *STRIPAK complex controls bFGF-induced collagen I invasion of MB cells*

111 STRIPAK complex members STRN4, STRN3, and STRIP1 are highly expressed in MB, and the
112 expression of STRNs correlates positively with site-specific phosphorylation of MAP4K4 in ID1 and
113 negatively with phosphorylation in ID2 *in vivo* ([32] and Figure S2A-D), suggesting a potential
114 contribution of these proteins to MAP4K4 regulation and MB pathogenesis. MAP4K4 promotes GF-

115 induced MB cell motility[9,10]. Hence, we tested the implication of STRIPAK complex proteins in
116 invasive motility in DAOY (SHH) MB cell lines by stable knockout (KO) of STRN4, STRN3, or STRIP1
117 (Figure S3A,B). Using the spheroid collagen I invasion assay (SIA[33]), we observed that STRN4 KO
118 abrogated bFGF-induced cell invasion in DAOY cells, while KO of either STRIP1 or STRN3 had little or
119 no effect (Figure S3C).

120 We next determined the effect of simultaneous depletion of various STRIPAK components on GF-
121 induced migration using siRNA (Figure S3D,E) in DAOY cells. siSTRN4 confirmed STRN4 implication
122 in bFGF-induced DAOY collagen I invasion, and siSTRN3 also reduced bFGF-induced invasion (Fig.
123 2A). In contrast, siSTRIP1 caused a marked increase in both EGF- and bFGF-induced dissemination.
124 Consistent with a functional redundancy of STRN3 and STRN4, we observed that combined depletion
125 of STRN3 and STRN4 had an additive effect on EGF- or bFGF-induced collagen I invasion. Thus,
126 STRN3 and STRN4 are, together with MAP4K4, required for GF-induced collagen I invasion in MB. We
127 confirmed the implication of STRIPAK components in migration control with another cell line, UW228,
128 an found that depletion of either MAP4K4, STRN4 or STRN3 reduced collagen I invasion (Figure 2B,
129 Figure S3F,G).

130 STRIPAK complex can regulate associated kinases by enabling dephosphorylation through the
131 PP2A catalytic subunit[34,35]. Inhibition of PP2A sensitizes tumors to radiation and/or chemotherapy
132 and attenuates cell migration[36,37]. We found that the PP2A inhibitor LB-100 decreased bFGF-induced
133 collagen I invasion in a dose-dependent manner (Figure 2C) without affecting cell viability (Figure S3H).
134 Thus, PP2A is not acting as a negative regulator of STRIPAK complex-associated MAP4K4 towards
135 GF-induced migration in MB cells, and STRN3/4 enable or facilitate the pro-invasive phenotype in GF-
136 stimulated MB cells.

137 *STRN3 controls GF-induced tissue expansion of tumor cell*

138 We used an *ex vivo* organotypic cerebellum slice culture model (OCSCs) to test STRIPAK implication
139 in MB tissue invasion (Figure S4A). OCSCs maintain key features of the normal cerebellum
140 cytoarchitecture and constitute a physiologically relevant microenvironment model[38], where FGFR
141 signaling contributes to MB growth and tissue invasion[6]. We first tested whether the depletion of
142 MAP4K4 or STRIPAK components prevented growth and tissue invasion of DAOY cells. We found that
143 STRN3 depletion caused a significant reduction of tumor area (Figure 3A). Treatment of the co-culture
144 with EGF enhanced brain tissue invasion of the tumor cells (Figure S4B,C). Depletion of MAP4K4

145 caused rounded cell morphology and moderately reduced EGF-induced invasion (Figure S4B-D).
146 Depletion of STRN3 caused compaction of the tumor cell spheroids and prevented tissue invasion also
147 under EGF-stimulation (Figure S4C,D). Conversely, depletion of STRIP1 induced a more infiltrative
148 behavior, similar to what was observed *in vitro* (Figure 2A). The combined depletion of MAP4K4 and
149 STRN3 in DAOY cells caused a dramatic reduction of tumor area, both under basal condition and under
150 EGF stimulation (Figure 3A,B, Figure S4B-D). The reduced tumor area in cells with combined depletion
151 is not the result of impaired proliferation, as remaining cells display proportionally similar EdU
152 incorporation as the control (Fig. S4E).

153 To confirm STRN3 implication in tissue invasion, we implanted HD-MBO3 group 3 MB cell lines KO
154 for either MAP4K4, STRN4, STRN3, or STRIP1 (Figure S3B) in OCSCs. HD-MBO3 cells are invasive
155 and display a high growth rate[38]. We observed a moderate for MAP4K4 KO and a significant reduction
156 in the expansion for STRN3 KO cell-derived tumors, both after five days in basal or GF-stimulated
157 conditions (Figure 3C,D, Figure S5). Moreover, the number of EdU-positive nuclei was considerably
158 reduced in sgSTRN3 and sgSTRN4 but not in sgMAP4K4 cells (Figure 3E).

159 This data supports a model of STRIPAK complex control of growth and invasion of MB tumor cells
160 in the cerebellum tissue environment.

161 *Opposing functions of STRN3/4 and MAP4K4 in cell proliferation and YAP/TAZ target gene regulation*

162 Depletion of STRN3 and STRN4 but not of MAP4K4 reduced MB cell growth in the cerebellum tissue.
163 We therefore tested the implication of MAP4K4 and of STRIPAK complex components in colony-
164 formation and clonal growth. Depletion of MAP4K4 caused a marked increase in colony number
165 independent of growth factor stimulation in DAOY cells (Figure 4A). Conversely, depletion of STRN3
166 impaired colony formation and clonal growth. Consistently, depletion of either STRN4 or STRN3 caused
167 a significant decrease in the number of HD-MB03 colonies (Figure 4B), demonstrating that an intact
168 STRIPAK complex and in particular STRN3 was necessary for clonal growth and colony expansion in
169 MB cells. The effect of STRN3 depletion was particularly striking under bFGF stimulation in HD-MB03
170 cells, which promoted massive colony-forming activity in this group 3 MB model (Figure 4B).

171 MAP4K4 is an activator of the Hippo tumor suppressor pathway, thereby repressing YAP/TAZ target
172 gene expression and growth[39,40]. By antagonizing these growth-repressive MAP4K4 functions, the
173 STRIPAK complex halts Hippo pathway activation and promotes YAP/TAZ transcriptional
174 activity[30,41,42]. We found that MAP4K4 depletion significantly increased the expression of the

175 YAP/TAZ target genes *CTGF*, *CYR61*, and *ANKRD1*, which supports a Hippo-pathway activating
176 function of MAP4K4 in MB cells (Figure 4C,D). Conversely, suppression of STRN3 or STRN4 decreased
177 transcription of these genes and also reverted the transcriptional activation induced by MAP4K4
178 depletion (Figure 4C). Thus, MAP4K4 blocks MB cell proliferation, possibly by promoting the activation
179 of the Hippo pathway, whereas the STRIPAK complex and, in particular, STRN3, antagonizes Hippo
180 activation and is necessary for proliferation of MB cells (Figure S6A).

181 STRIPAK phosphatase PP2A antagonizes different Hippo kinases and thereby suppresses the
182 Hippo tumor-suppressing activity and promotes a YAP/TAZ transcriptional program[30,43].
183 Consistently, PP2A inhibitor LB-100 repressed transcription of YAP/TAZ target genes (Fig. 4E).
184 However, depletion of MAP4K4 restored YAP/TAZ target gene expression under LB-100 treatment,
185 indicating that PP2A acts as a negative regulator of MAP4K4 function towards Hippo pathway activation
186 (Figure 4E, Figure S6B). Furthermore, we found that bFGF stimulation promotes YAP/TAZ target genes
187 expression in DAOY and HD-MBO3 cells. This increased YAP/TAZ target gene expression requires
188 active PP2A and STRN3 (Figure 4F,G, Figure S6C,D), suggesting that STRN3 functions as Hippo
189 pathway antagonist in FGFR-activated MB cells by enabling PP2A-mediated repression of MAP4K4
190 (Figure 4E-G, Figure S6B-D).

191 *Novel protein kinases C are downstream effectors of MAP4K4 and STRN3 in promigratory signaling*

192 To identify effectors of MAP4K4 and of STRIPAK complex components downstream of FGFR
193 activation, we profiled changes in global kinase activities using the PamGene array technology. FGFR
194 signaling caused significantly increased activities of CDKs, PKC, SRC kinases, and FAK (Figure 5A,
195 Figure S7A). Several of these and additional bFGF-induced kinase activities require the expression of
196 MAP4K4 or of STRIPAK complex components (Figure 5A, Figure S7A). The most differently regulated
197 Ser/Thr (STK) kinases cluster in the AGC (cAMP-dependent, cGMP-dependent, and PKC) family of
198 kinases (Figure S7B-E). The activities of several AGC kinases were reduced when MAP4K4, STRN4,
199 or STRN3 were downregulated, and increased in STRIP1-depleted cells. Moreover, STRIP1 depletion
200 increased the activity of a MAP4K4 signature (Figure 5A), indicating that STRIP1 represses MAP4K4 in
201 MB cells. Interestingly, depletion of MAP4K4, STRN3 or STRN4, but not of STRIP1, caused a striking
202 decrease in bFGF-induced activity signature of “novel” protein kinases C (nPKCs, PKCδ, ε, η and θ)
203 (Figure 5A). This suggested that MAP4K4 and STRIPAK components are necessary for bFGF-induced
204 activation of nPKCs. Indeed, by IB analysis we could demonstrate that depletion of MAP4K4 or of

205 STRN3 reduced T538 phosphorylation of the catalytic domain of PKCθ (Figure 5B), which suggested
206 that MAP4K4 and STRN3 promote the activation of PKCθ[44].
207 Activated nPKCs could constitute druggable effector kinases to repress MB cell dissemination. We
208 tested this possibility using inhibitors specific for PKCθ (PKCθi[45] and Darovasertib[46]). We observed
209 a dose-dependent reduction of bFGF-induced cell dissemination in DAOY cells (Figure 5C, Figure S8A).
210 A similar effect was obtained using the PKCδ inhibitor Rottlerin (Figure S8B)[47]. Notably, the inhibition
211 of classical PKCα, β, γ kinases by Bisindolylmaleimide I (BIM) did not significantly repress MB cell
212 dissemination (Figure S8C). PKCθ or PKCδ inhibition also resulted in the compaction of DAOY and HD-
213 MBO3 tumor spheroids in the OCSC model and in the reduction of cerebellum tissue invasion, without
214 affecting MB cell proliferation (Figure 5D-F, Figure S8D-F). Depletion of PKCθ by siRNA (Figure S8G,H)
215 confirmed its implication in bFGF-induced DAOY collagen I invasion (Figure 5G). Moreover, PKCθ
216 depletion abolished bFGF-induced cerebellum tissue invasion of DAOY and HD-MBO3 cells (Figure
217 5H,I, Figure S8I,J).
218 Collectively these data demonstrate that MAP4K4 and STRN3 promote a pro-migratory phenotype
219 in MB cells through the activation of common downstream effectors, which include novel but not classical
220 PKC family members.

221 *MAP4K4 and STRN3 enable bFGF-induced VASP Ser157 phosphorylation*

222 Depletion of MAP4K4 in bFGF-stimulated DAOY cells resulted in an overall decrease in the
223 phosphorylation of multiple STK and PTK consensus phosphorylation sites (Figure 6A, Figure S9A,B,
224 Table S3). Many of these alterations were phenocopied by the depletion of STRN3 (Figure 6A).
225 Conversely, depletion of STRIP1 caused a global increase in the phosphorylation of STK substrates
226 (Figure 6A, Figure S9A). Phosphorylation profiles of PTK substrates were similar under all conditions
227 (Figure 6A, Figure S9B), with 23 substrates uniquely altered by MAP4K4 or STRN3 depletion (Figure
228 6B), including the phospholipase C-γ (PLC-γ)-binding site[48] of FGFR1 ($FGFR_{Y766}$), and the SRC
229 phosphorylation site of AKT (AKT_{Y326})[49] (Figure 6C). Additionally, we observed the reduction of
230 $FAK1_{Y570/576}$ phosphorylation in siMAP4K4 and siSTRN3, supporting the previously described role of
231 MAP4K4 in mediating FAK protein activation and focal adhesion assembly[10] (Figure 6C).
232 Exploring potential direct substrates of MAP4K4, we found that both MAP4K4 and STRN3 depletion
233 decreased the phosphorylation of $VASP_{S157}$ (Figure 6C), an F-actin elongation promoting factor[50,51].
234 Phosphorylation of S157 enables VASP translocation to the plasma membrane at the leading edge of

235 migrating cells[52,53] and regulates anti-capping activity[51]. In bFGF-stimulated cells, VASP
236 accumulated in the cortical cytoskeleton and the plasma membrane (Figure 6D), and in cells invading
237 the brain tissue, we observed filopodia-like protrusions only in control but not in MAP4K4 or STRN3-
238 depleted cells (Figure S9C). Consistently, depletion of MAP4K4 or of STRN3 caused a robust reduction
239 of bFGF-induced $VASP_{S157}$ phosphorylation in cells seeded on collagen I matrix (Figure 6E). Under the
240 same condition, $VASP_{S157}$ phosphorylation is repressed by the MAP4K4 inhibitor GNE-495 in DAOY
241 and HD-MBO3 cells (Figure S9D,E), supporting the notion that MAP4K4 directly phosphorylates this
242 residue both under basal condition as well as in response to FGFR activation. Overexpression of full-
243 length MAP4K4 increased bFGF-induced $VASP_{S157}$ phosphorylation (Figure 6F). No increased
244 $VASP_{S157}$ phosphorylation was observed in cells overexpressing a C-terminally truncated MAP4K4 (KD-
245 ID1-ID2-FLAG, Figure 1H) or depleted of STRN3 (Figure 6F,G). To test whether the MAP4K4-STRN3
246 complex is able to directly phosphorylate recombinant VASP, we performed an *in vitro* kinase assay
247 using bacterially expressed VASP protein. MAP4K4 immunoprecipitated from bFGF stimulated cells
248 caused increased $VASP_{S157}$ phosphorylation *in vitro* (Figure 6G). We observed no increase in $VASP_{S157}$
249 phosphorylation when MAP4K4 is immunoprecipitated from STRN3-depleted cells, suggesting that
250 STRN3 is necessary to either activate MAP4K4 or to couple it to the VASP protein (Figure 6G). To test
251 the implication of VASP in bFGF-induced invasiveness in MB cells, we assessed siRNA-depletion of
252 VASP using the SIA (Figure S9F,G). We found that VASP depletion causes a significant but only partial
253 reduction of bFGF-induced collagen invasion (Figure 6H).

254 Taken together, these data identified $VASP_{S157}$ phosphorylation as a novel direct effector mechanism
255 of MAP4K4 and STRN3 downstream of FGFR signaling and highlighted VASP as a mediator of bFGF-
256 induced MB cell invasion.

257 Discussion

258 We found that MAP4K4 interacts with the STRIPAK complex, and that this interaction orchestrates
259 growth and invasion control downstream of FGFR signaling in MB cells (Fig. 7). Mechanistically,
260 MAP4K4 interaction with STRN3 and STRN4 represses MAP4K4 activity towards Hippo tumor
261 suppressor pathway activation by bringing the kinase in proximity of PP2A, which stalls MAP4K4
262 repression of YAP/TAZ target gene expression. Conversely, STRN3 and MAP4K4 interaction is
263 necessary for the activation of PKCθ and VASP, which we found to promote invasion downstream of

264 activated FGFR in MB. This axis of STRIPAK complex function is not repressed by PP2A. We
265 furthermore revealed direct phosphorylation of VASP by MAP4K4 and found that VASP phosphorylation
266 by MAP4K4 requires its interaction with STRN3. Thus, MAP4K4-mediated activation of PKCθ and VASP
267 constitute a molecular link between the STRIPAK complex and the control of cytoskeleton dynamics.
268 With this, the STRIPAK complex may balance the dichotomous functionality of MAP4K4 towards
269 increased invasion and reduced growth repression in MB and other FGFR-driven tumors.

270 The interaction of the STRIPAK complex with MAP4K4 confirms previous findings describing a direct
271 interaction of STRIPAK with MST1/2, MST3/4, and MAP4Ks[19,25,34,35] in a brain tumor, where
272 MAP4K4 is highly expressed. MAP4K4 is a Hippo pathway kinase that through the direct
273 phosphorylation of LATS1/2 caused repression of YAP/TAZ transcriptional activity. The STRIPAK
274 complex promotes PP2A-mediated inactivation of MAP4K4 and thereby antagonizes Hippo
275 signaling[30,39,42]. We confirmed this canonical function of MAP4K4 and of STRIPAK [30,41,42,54]
276 and furthermore demonstrated that MAP4K4 depletion increases colony formation and clonal growth in
277 two different MB tumor cell models. From these findings, we conclude that MAP4K4 and STRN3/4 have
278 opposing functions towards Hippo signaling in MB, and that the STRIPAK complex exerts a growth-
279 promoting function by suppressing the corresponding activity of MAP4K4 through the phosphatase
280 PP2A in MB cells.

281 Parallel to antagonistic proliferation regulation of MAP4K4 and STRN3/4, we discovered that
282 MAP4K4 and STRN3 display a co-operative function towards bFGF-induced invasion control. We
283 identified AGC kinases and, in particular, novel PKCs (nPKCs), which are known promoters of
284 tumorigenesis[55], as downstream effectors of MAP4K and STRN3 in invasion control, complementing
285 previous reports of tumor invasion control by STRIPAK with mechanistic insight[26,56]. bFGF-driven
286 invasion in MB may additionally involve the activation of adhesion and cytoskeleton-associated proteins
287 like ezrin- radixin-moesin (ERM), β1 integrin, and focal adhesion kinase (FAK)[57–61], the activity of
288 latter we also found increased by bFGF in a MAP4K4 and STRN3/4-dependent manner. The activation
289 of nPKCs can be induced downstream of RTKs through phospholipase Cγ (PLCγ) signaling[62]. PLCγ
290 is activated by its association with the phosphorylated Y766 residue of the activated FGFR[48].
291 Depletion of either MAP4K4 or of STRN3 not only decreased the nPKC activity signature but also
292 decreased the phosphorylation of the Y766 residue on FGFR1. This indicates that regulation of Y766
293 phosphorylation could mechanistically link MAP4K4-STRIPAK function to PKC activation downstream

294 of bFGF stimulation. Specific targeting of PKCδ and PKCθ may thus contribute to an effective blockade
295 of FGFR-driven invasiveness in MB and other FGFR-driven tumors.

296 STRN3 and MAP4K4 are necessary for maintaining an elongated, mesenchymal motility mode in the
297 brain tissue, and cells devoid of STRN3 or of MAP4K4 display a rounded morphology that expresses
298 fewer filopodia-like protrusions. The involvement of MAP4K4 and STRIPAK complex members in
299 regulating the actomyosin cytoskeleton has been addressed in several studies[11,24]. However, the
300 interplay of MAP4K4 and the STRIPAK complex in cytoskeleton remodeling towards cancer cell
301 dissemination has not been addressed and a direct substrate of MAP4K4 in this process not identified.
302 Therefore, we consider the phosphorylation of $VASP_{S157}$ by MAP4K4 particularly relevant, because
303 phosphorylation of this residue could couple STRIPAK complex function to VASP localization,
304 cytoskeleton regulation, and cell migration[51,52]. MAP4K4-dependent $VASP_{Ser157}$ phosphorylation may
305 contribute to GF-induced MB cell motility and invasion by promoting cytoskeleton remodeling and the
306 formation of membrane protrusions. In support of this is our observation in previous studies[6] and herein
307 that tissue-invading MB tumor cells display filopodia-like protrusions, and that loss of these protrusions
308 is associated with reduced invasion. MAP4K4 phosphorylation of $VASP_{Ser157}$ *in vitro* depends on
309 MAP4K4 co-purification with STRN3, implying that VASP is a direct substrate of MAP4K4 and that
310 STRN3 is necessary for productive VASP phosphorylation by MAP4K4. It is possible that STRN3 brings
311 VASP and MAP4K4 in proximity. VASP was pulled down specifically by N-BioID2-M4K4 but not C-
312 BioID2-M4K4, indicating that VASP localizes in the proximity of the kinase domain of MAP4K4 in cells.
313 MAP4K4 and STRN3 also promote the activity of several AGC kinases that are implicated in $VASP_{Ser157}$
314 phosphorylation, like PKG and PKD1[63], which could act as additional VASP kinases downstream of
315 MAP4K4 in MB cells. Depletion of VASP caused a moderate reduction (-25%) of bFGF-induced collagen
316 I invasion. This indicates that VASP is unlikely the main driver of invasion control in MB. However,
317 additional functions of VASP in tumorigenesis argue for further clarification of the implication of $VASP_{S157}$
318 phosphorylation by MAP4K4 in MB.

319 Depletion of STRIP1 moderately increased GF-induced migration and tissue invasion in MB. The
320 increase in the MAP4K4 kinase activity signature after STRIP1 depletion further supports the notion of
321 an antagonizing function of STRIP1 towards MAP4K4. However, the lack of a clear phenotype after
322 STRIP1 depletion also indicates only a minor contribution to migration and growth control in MB tumor
323 cells. STRIP1 depletion has been associated with a contractile motility mode, supporting migration in

324 confined, stiff spaces[64]. Rounded, blebbing motility may contribute to brain invasion, albeit at lower
325 efficacy, and we previously observed a similar phenomenon in cells treated with the SRC-BCR/ABL
326 inhibitor dasatinib, which represses mesenchymal migration[65].

327 Together, our data indicate that the cooperation of MAP4K4 and STRN3 promotes motility in a 3D
328 environment and in the brain tissue. This motility depends in part on the activation of novel PKCs and
329 on the phosphorylation of VASP, which in concert with the previously identified regulation of ERM
330 proteins and the Arp2/3 complex by MAP4K4[10,17,18], may promote invasive motility in environments
331 of variable complexity and stiffness.

332 In conclusion, we found that MAP4K4 exerts pro-invasive and anti-proliferative activities in MB cells
333 and that STRN3 contributes to and modulates these MAP4K4 functions downstream of FGFR signaling.
334 This dichotomous functionality of MAP4K4 in tumor cells provides an explanation why MAP4K4
335 depletion alone is not sufficient to shrink the tumor volume *ex vivo,* despite the anti-invasive activity of
336 this treatment. Remarkably, however, co-depletion of MAP4K4 and STRN3 caused a near-complete
337 eradication of the tumor cells and completely abrogated cell dissemination *in vitro*. These findings argue
338 strongly for the development of STRN3 targeting strategies as therapeutic interventions to block MB cell
339 proliferation and invasion. Peptide disruption of the STRN3-PP2A interaction has anti-tumor effects by
340 impairing the phosphatase inactivation of the kinase in the complex and concomitant hippo pathway
341 activation[66]. However, PP2A inhibition repressed invasion in MB cells in a dose-dependent manner,
342 indicating that STRIPAK-associated PP2A is rather unlikely to repress MAP4K4 pro-invasive activity.
343 Rather, targeting of the cooperation of STRN3 and MAP4K4 to repress the pro-invasive activities of
344 MAP4K4 and to unleash its anti-proliferative functions through Hippo pathway activation could represent
345 a successful strategy to impair both MB cell proliferation and spreading. YAP/TAZ target gene
346 expression and the phosphorylation status of their common downstream effectors PKCθ and VASP in
347 patient samples may inform clinicians in the future about the potential susceptibility to therapies targeting
348 this pathway.

349

350 ## Material and methods

351 ***Reagents***

352 Protein phosphatase PP2A inhibitor LB-100 (S7537), PKC-θ inhibitor (S6577), Darovasertib (S6723),
353 Rottlerin (S7862), and Bisindolylmaleimide I (S7208) were purchased from Selleckchem, Houston, TX,
354 USA. MAP4K4 inhibitor GNE-495 was kindly provided by Genentech Inc.[67]. EGF (100-47) and bFGF
355 (100-18B) were purchased from PeproTech, London, UK. If not otherwise indicated, the cells were
356 treated with growth factors at these concentrations: EGF: 30 ng/ml, bFGF: 100 ng/ml.

357 ***Cells and cell culture***

358 DAOY human MB cells were purchased from the American Type Culture Collection (ATCC, Rockville,
359 MD, USA) and cultured in Iscove's Modified Dulbecco's Medium (IMEM, Sigma). UW228 cells were
360 generously provided by John Silber (Seattle, USA) and cultured in Dulbecco's Modified Eagle Medium
361 (DMEM, Sigma). HD-MBO3 group 3 MB cells were generously provided by Till Milde (DKFZ, Germany)
362 and cultured in RPMI medium (Sigma). Human embryonic kidney HEK-293T cells were cultured in
363 Dulbecco's modified Eagle's medium (DMEM, Sigma). Cell culture media were supplemented with 10%
364 fetal bovine serum (FBS, Sigma), 1% Penicillin-Streptomycin (ThermoFisher Scientific), and 1%
365 GlutaMAX (Gibco). DAOY LA-EGFP and HD-MBO3 LA-EGFP cells were produced by lentiviral
366 transduction of DAOY and HD-MBO3 cells with pLenti-LA-EGFP. The cells were maintained at 37°C in
367 a humidified atmosphere containing 5% CO_2. All cells were confirmed to be mycoplasma negative. Cell
368 line authentication and cross-contamination testing were performed by Multiplexion by single nucleotide
369 polymorphism (SNP) profiling.

370 ***Plasmids***

371 Lentiviral constructs were ordered from VectorBuilder (Santa Clara, CA, USA). For BioID experiments,
372 3xFLAG-tagged BioID2 biotin ligase was fused to either the N-terminus (3xFLAG-BioID2-MAP4K4) or
373 the C-terminus (MAP4K4-BioID2-3xFLAG) of human MAP4K4 cDNA (NM_145686.4). An extended
374 flexible linker consisting of 13 repeats of GGGGS was inserted between MAP4K4 and the BioID2
375 ligase[27]. As negative controls, only BioID2-FLAG was used. Details of the vectors can be found at
376 https://en.vectorbuilder.com/vector/VB180410-1463qqf.html (N-BioID-MAP4K4),
377 https://en.vectorbuilder.com/vector/VB180410-1356dmp.html (C-BioID2-MAP4K4), and
378 https://en.vectorbuilder.com/vector/VB180411-1121jky.html (BioID2-CTRL). See also Figure S1. For

379 the analysis of MAP4K4 domains, we designed different constructs encoding 3xFLAG-tagged truncated
380 versions of MAP4K4 cDNA (Figure 1j). Details of the vector can be found at:
381 https://en.vectorbuilder.com/vector/VB190724-1021fsg.html (full-length MAP4K4),
382 https://en.vectorbuilder.com/vector/VB190724-1072aza.html (ID1-ID2-CNH, residues 290-1273),
383 https://en.vectorbuilder.com/vector/VB190724-1048drb.html (KD, residues 1-289),
384 https://en.vectorbuilder.com/vector/VB190724-1089brg.html (KD-ID1-ID2, residues 1-954),
385 https://en.vectorbuilder.com/vector/VB190724-1058sct.html (ID1, residues 290-634), and
386 https://en.vectorbuilder.com/vector/VB190724-1062xrk.html (ID2, residues 635-954). All plasmids were
387 verified by Sanger sequencing.

388 ***Mouse maintenance***

389 Mouse protocols for organotypic brain slice culture were approved by the Veterinary Office of the Canton
390 Zürich (Approvals ZH134/17, ZH116/20). Wild type C57BL/6JRj pregnant females were purchased from
391 Janvier Labs and were kept in the animal facilities of the University of Zürich Laboratory Animal Center.

392 ***Immunoblotting (IB)***

393 To analyze total cell lysates by immunoblot, 1 x 10^5 DAOY wild type or 2.5 x 10^5 HD-MBO3 cells were
394 lysed using RIPA buffer supplemented with protease (Complete Mini, Roche) and phosphatase
395 inhibitors (PhosSTOP, Roche) and cleared by centrifugation. Protein concentration was assessed using
396 the Pierce BCA Protein Assay Kit (Thermo Fisher Scientific) according to the manufacturer's
397 instructions. Protein separation was performed on Mini-Protean TGX (4-15% or 4-20%) SDS-PAGE gel
398 (Bio-Rad) and transferred to PVDF membranes (Bio-Rad). After 1 h of blocking with 5% non-fat milk,
399 membranes were probed with primary antibodies listed in Supplementary material (Table 1). GAPDH or
400 β-tubulin were used as internal loading control. HRP-linked secondary antibodies (1:5000) were used
401 to detect the primary antibodies. Chemiluminescence detection was carried out using ChemiDoc Touch
402 Gel and Western Blot imaging system (Bio-Rad). The integrated density of immuno-reactive bands was
403 quantified using ImageJ (National Institutes of Health, USA).
404 To assess PKCθ T538 and VASP S157 phosphorylation, the cells were seeded on a collagen-coated
405 plate and starved for 16 h before treatment with growth factors and inhibitors. Protein extraction was
406 performed by directly incubating the cells at 95°C for 5 minutes with a lysis buffer containing 2.5% SDS

407 and 125 mM Tris-HCl pH 6.8 supplemented with protease and phosphatase inhibitors. The lysates were
408 resolved by SDS-PAGE and analyzed by IB as described above.

409 ***Biotin-streptavidin affinity purification***

410 The protocol for isolating proteins biotinylated by biotin ligase was adapted from the BioID method
411 [27,29]. For proximity-labeling experiments with HEK-293T, 7 x 10^6 cells were transiently transfected
412 with N-BioID2-M4K4, C-BioID2-M4K4, or BioID2-CTRL plasmids using jetPRIME reagent (Polyplus
413 Transfection) according to manufacturers' instructions. Non-transfected WT HEK-293T cells were used
414 as a negative control (to exclude biotin-independent binders). Twenty-four hours after the transfection,
415 the cells were incubated with 50 µM biotin for 16 h. For proximity-labeling experiments with DAOY MB
416 cells, we generated cells stably transfected with N-BioID2-M4K4, C-BioID2-M4K4, or BioID2-CTRL
417 lentivirus. 5 x 10^6 cells were incubated with biotin as above. Parental WT DAOY cells were used as a
418 negative control. After 16 h of biotin incubation and two PBS washes, the cells were lysed at 4°C with 1
419 ml of lysis buffer containing 50 mM Tris-HCl (pH 7.5), 150 nM NaCl, 1 mM EDTA, 1 mM EGTA, 1%
420 Triton X-100, 0.1% SDS and protease inhibitor tablet (Roche). The protein concentrations were
421 normalized among the samples. Two mg of protein samples were incubated with 75 µl of pre-equilibrated
422 Dynabeads MyOne Streptavidin T1 magnetic beads (65602, Thermo Fisher Scientific) in low-binding
423 Eppendorf tubes. The mixtures were incubated for 3 h at 4 °C with end-over-end rotation. The beads
424 were collected using a magnetic rack and washed twice with lysis buffer and twice with 50 mM
425 ammonium bicarbonate (pH 8.3). 10% of the streptavidin-conjugated beads were used for
426 immunoblotting. Proteins were eluted by heating the beads at 95°C for 5 min in Laemmli Sample Buffer
427 (1610747, Bio-Rad) with 50 mM DTT followed by magnetic separation. The remaining beads with bound
428 proteins were transferred to a fresh centrifuge tube, resuspend in 150 µl of 50 mM ammonium
429 bicarbonate, and used for MS analysis. For each condition, three biological replicates were performed
430 and analyzed by MS.

431 ***Mass spectrometry (MS)***

432 Tryptic digestion of proteins isolated by streptavidin pull-down was performed based on the protocol
433 described in[28]. Data acquisition was performed by the Functional Genomics Center Zurich (FGCZ). In
434 brief, 50 µl of 8 M urea were added to 150 µl of bead-protein suspensions in 50 mM ammonium
435 bicarbonate (pH 8.3). Beads were reduced by adding 4 µl of 100 mM Tris (2-carboxyethyl) phosphine

436 (TCEP), alkylated with 4 µl of 500 mM chloroacetamide (CAA) and incubated at 30°C for 1 h in the dark
437 using an Eppendorf Thermomixer at 700 rpm. Sample volume was adjusted by adding 200 µl of digest
438 buffer (10 mM Tris-HCl, 2 mM $CaCl_2$, pH 8.2) to dilute the 8 M urea to 1 M before trypsin digestion. The
439 mixture was treated with 1 µg/sample trypsin and incubated for overnight digestion in the dark at 30°C
440 using an Eppendorf Thermomixer at 1000 rpm. The supernatant was collected in a fresh Eppendorf tube
441 after magnetic separation of the beads. The beads were washed twice with 100 µl 10 mM Tris-HCl pH
442 8.2/10% acetonitrile. These washes were pooled with the first eluate and acidified with 60 µl 5%
443 trifluoroacetic acid (TFA, final concentration 0.5%). The samples were desalted on Sep-Pack C18
444 columns (Thermo Scientific), completely dried using speed vac centrifugation, and dissolved in 20 µl
445 0.1% formic acid (FA). The samples were diluted 10-fold and transferred to autosampler vials for liquid
446 chromatography-tandem mass spectrometry (LC-MS/MS). 2 µl of samples were injected by an Easy-
447 nLC 1000 system (Thermo Scientific) and separated on an EasySpray-column (75 µm x 500 mm)
448 packed with C18 material (PepMap, C18, 100 Å, 2 µm, Thermo Scientific). The column was equilibrated
449 with 100% solvent A (0.1% FA in water). The column was equilibrated with 100% solvent A (0.1% FA in
450 water). Peptides were eluted using the following gradient of solvent B (0.1% FA in acetonitrile): 5-25%
451 B in, 60 min; 25-35% B in 10 min; 35-99% B in 5 min at a flow rate of 0.3 µl/min. All precursor signals
452 were recorded in the Orbitrap using quadrupole transmission in the mass range of 300-1500 m/z.
453 Spectra were recorded with a resolution of 120 000 at 200 m/z, a target value of 5E5 and the maximum
454 cycle time was set to 3 seconds. Data dependent MS/MS were recorded in the linear ion trap using
455 quadrupole isolation with a window of 1.6 Da and HCD fragmentation with 30% fragmentation energy.
456 The ion trap was operated in rapid scan mode with a target value of 8E3 and a maximum injection time
457 of 80 ms. Precursor signals were selected for fragmentation with a charge state from +2 to +7 and a
458 signal intensity of at least 5E3. A dynamic exclusion list was used for 25 seconds. The mass
459 spectrometry proteomics data were handled using the local laboratory information management system
460 (LIMS).

461 ***Proteomic data analysis***

462 The MS/MS raw data of three biological replicates were combined and searched against a SwissProt
463 database with *Homo sapiens* taxonomy using Mascot (version 2.6.2, London, UK), with a parent ion
464 tolerance of 10 ppm and a fragment ion mass tolerance of 0.030 Da. The database was also expanded
465 with frequently observed contaminants, such as bovine serum albumin, trypsin, and keratins

466 carbamidomethylation of cysteine residues (C) was specified as a fixed modification and oxidation of
467 methionine (M) was set as a variable modification. Scaffold (version 4.8.9, Proteome Software Inc.,
468 Portland, OR) was used to validate MS/MS-based peptide and protein identifications. 1% and 0.1% false
469 discovery rate (FDR) cutoff on peptide and protein, respectively, was used to control for false
470 identifications. Protein identifications were accepted if they contained at least 2 identified peptides per
471 protein. Proteins that contained similar peptides and could not be differentiated based on MS/MS
472 analysis alone were grouped to satisfy the principles of parsimony. Proteins sharing significant peptide
473 evidence were grouped into clusters. Proteins detected in the parental control samples (WT cells lacking
474 BioID2 expression) were subtracted from the results. The significance of enrichment was tested using
475 a two-tailed student's *t*-test with equal variances. Hits were considered significantly enriched in
476 MAP4K4-BioID2 cells compared the unspecific background (BioID2-CTRL) if they had > 2-fold
477 enrichment and p-values < 0.05. Gene ontology (GO) enrichment analysis of MAP4K4-interacting
478 partners was performed using Metascape (http://metascape.org/) [68]. All relevant data have been
479 deposited to the ProteomeXchange Consortium via the PRIDE (http://www.ebi.ac.uk/pride) partner
480 repository with the data set identifier PXD031863 and 10.6019/PXD031863 for the MAP4K4 interactome
481 in HEK293T cells and PXD031870 and 10.6019/PXD031870 for for the MAP4K4 interactome in DAOY
482 cells.

483 ***Co-immunoprecipitation (Co-IP)***

484 2.5 x 10^6 DAOY or 3.5 x 10^6 HEK-293T cells were lysed at 4°C with 400 µl of buffer containing 50 mM
485 Tris-HCl (pH 7.5), 150 nM NaCl, 0.3% NP-40 with protease and phosphatase inhibitor cocktail. Lysates
486 were cleared by centrifugation, and protein concentrations were normalized among the samples. For
487 immunoprecipitation, 30 µl of Dynabeads Protein G magnetic beads (10004D, Thermo Fisher Scientific)
488 were coated with 3 µg of specific antibody or control IgG by resuspending them in 60 µl PBS containing
489 0.02% Tween-20 (P1379, Sigma), and rotated for 45 min at 4°C. 1 mg of protein samples was incubated
490 with the antibody-coated Dynabeads for 3 h at 4 °C with end-over-end rotation. The beads were washed
491 four times with TBS buffer (50 mM Tris-HCl pH 7.4, 150 mM NaCl). The proteins were eluted by
492 incubating the beads with 35 µl 100 µg/ml 3xFLAG-Peptide (F4799, Sigma Aldrich) at room temperature
493 for 20 min or by adding Laemmli Sample Buffer (1610747, Bio-Rad) containing 50 mM DTT and
494 denaturation at 95°C for 5 min. The beads were then magnetically separated from the eluates and the
495 samples analyzed by IB as described above.

496 ***Immunofluorescence analysis (IFA)***

497 To visualize MAP4K4-BioID2 proteins, stably transduced DAOY cells were plated on glass coverslips
498 and incubated with 50 µM biotin for 16 h. The cells were fixed and permeabilized as described in[69].
499 The fixed cells were incubated with Streptavidin Alexa Fluor 594 conjugate (Invitrogen) for 1.5 h at RT,
500 followed by incubation with primary antibodies overnight at 4°C. Secondary antibodies were incubated
501 for 2 h at RT.

502 For VASP localization analysis, 2000 LA-EGFP DAOY cells were seeded in a 384 well plate (781090,
503 Greiner Bio-One) coated overnight with 0.07 µg/µl collagen I (5005-B, Cell systems) diluted in 70%
504 EtOH. After seeding, the cells were starved for 16 h and treated with 100 ng/ml bFGF for 15 min. Cells
505 were fixed and incubated with primary and secondary antibodies as described above.

506 Imaging acquisition was performed using an SP8 confocal microscope (Leica). The list of the primary
507 and secondary antibodies used is provided in Supplementary material (Table 1). IFA Metadata can be
508 found in table S4.

509 ***Lentivirus Production and Transduction***

510 Lentiviral particles were produced by transfection of HEK-293T cells with transfer plasmids, psPAX2
511 (#12260, Addgene) and pCMV-VSV-G plasmids (#8454, Addgene)[70] in a ratio of 5:3:2 using
512 polyethylenimine (24765-2, Polysciences). Virus supernatant was harvested 30 h after transfection,
513 filtered, and concentrated using Amicon Ultra 15 ml Centrifugal Filters (Millipore). For the transduction,
514 human MB cells were incubated for 24 hours with supernatant containing the viral particles and 8
515 µg/ml polybrene. Two days after transduction, cells were selected with puromycin (DAOY: 2 µg/ml, HD-
516 MBO3: 1 µg/ml).

517 ***Generation of CRISPR/Cas9-mediated knockout cells***

518 Gene-specific single-guide RNA (sgRNAs) were designed using the online design tool at
519 https://design.synthego.com. Only highly specific target sites were selected, and the respective
520 sequences are listed in Supplementary material (Table 2). Oligonucleotides specific for the target sites
521 were synthesized with BsmBI restriction site overhangs by Microsynth (Balgach, Switzerland) and
522 cloned into the LentiCRISPRv2 transfer plasmid (Addgene plasmid #52961) with a single tube restriction
523 and ligation method as described in[71]. Production of lentiviral vectors and cell transduction was
524 performed as described above. The efficiency of the knockouts was tested by immunoblot.

525 ***RNA interference***

526 DAOY, UW228, or HD-MBO3 cells at approximately 70% confluency were transfected with
527 DharmaFECT Transfection Reagent 4 (T-2004-03, Dharmacon) or Lipofectamine RNAiMAX
528 Transfection Reagent (13778075, Thermo Fisher Scientific) with 10 nM siRNAs following the
529 manufacturer's instruction. The list of the siRNA used is provided in Supplementary material (Table 3).
530 Non-Targeting Control siRNA (siCTRL, D-001210-02-05, Dharmacon) was used as a negative control
531 for siRNA transfection. After 48 or 72 hours, RNA and proteins were isolated from the cells to determine
532 gene expression by qRT-PCR and to evaluate protein expression by IB. For SIA or organotypic
533 cerebellum slice culture experiements, the cells were re-seeded to form spheroids in ultra-low adhesion
534 plates 24 h after the transfection.

535 ***RNA extraction and quantitative Real-Time PCR (qRT-PCR)***

536 Total RNA was isolated from cells with the RNeasy mini kit (74106, Qiagen). cDNA was obtained by
537 retro-transcription of 1 µg total RNA using High-capacity cDNA Reverse Transcription Kit (4368813,
538 Applied Biosystems). qRT-PCR was performed using PowerUp Syber Green (A25776, Thermo
539 Scientific) under conditions optimized for the 7900HT Fast Real-Time PCR System (Applied
540 Biosystems). The primers used were synthesized by Microsynth AG (Balgach, Switzerland). Primer
541 sequences are detailed in Supplementary material (Table 4). The relative expression levels of each
542 gene of interest were calculated using the $2^{-\Delta\Delta Ct}$ method normalized to 18s.

543 ***Spheroid invasion assay (SIA)***

544 SIA was performed and quantified according to[33]. In brief: 2500 cells/100 µl per well were seeded in
545 cell-repellent 96 well microplates (650970, Greiner Bio-One, Kremsmünster, Austria). The cells were
546 incubated at 37°C for 24 h to form spheroids. 70 µl medium was removed and replaced with 70 µl of a
547 solution containing 2.5% bovine collagen I (CellSystems, Troisdorf, Germany). Polymerized collagen I
548 hydrogels were overlaid with 100 µl of serum-free media containing growth factors and/or inhibitors 2x
549 concentrated. The cells were allowed to invade the collagen matrix for 24 h, after which they were
550 stained with Hoechst (1:2000, B2883, Sigma Aldrich) for 3-4 h. Images were acquired with an
551 AxioObserver 2 mot plus fluorescence microscope (Zeiss, Munich, Germany) or with an Operetta high-
552 content imaging system (PerkinElmer) at 5x magnification. When acquired with the Operetta
553 microscope, the spheroids were localized in the well by acquiring 3 z-planes with 250 µm z-spacing, re-

554 scanned by acquiring 16 z-planes with 25 µm z-spacing and a maximum intensity projection was
555 computed and used for further analysis. Spheroids and invading cells were delineated based on
556 fluorescence threshold. Cell invasion was determined as the sum of the distance invaded by the cells
557 from the center of the spheroid as quantified using an automated cell dissemination counter (aCDc)[33]
558 or using Harmony 4.5 software (PerkinElmer).

559 ***Colony formation assay***

560 DAOY (400 cells/well) or HD-MBO3 (600 cells/well) cells were seeded in a 6-well plate in complete
561 growth medium containing 10% FBS. The cells were allowed to adhere for 48 h, and the medium was
562 replaced with fresh growth medium containing 1% FBS ± bFGF. The cells were cultured at 37°C for 10
563 days (DAOY) or 15 days (HD-MBO3) with medium changes every third or fourth day. The colonies were
564 fixed in methanol for 10 min at -20°C and then stained with 0.5% crystal violet for 15 min. The number
565 and the area of the colonies were quantified by ImageJ using the plugin colony area.

566 ***CellTox green cytotoxicity assay***

567 Cytotoxicity was determined using the CellTox™ Green Cytotoxicity Assay (G8742, Promega,
568 Dübendorf, Switzerland), according to manufacturer's instructions. 2500 DAOY cells were seeded in
569 100 µl per well of complete medium in 96-well Corning black wall microplates with clear round bottom
570 (Corning Incorporated, NY, USA). The cells were incubated at 37°C for 24 h to form spheroids. 50 µl of
571 the medium were then removed from each well and replaced with 50 µL of fresh medium containing
572 1:500 of CellTox™ Green Dye and different drug concentrations. Wells with medium but without cells
573 were used to measure background fluorescence. The fluorescence representing nonviable cells was
574 measured after 24, 48, and 72 h of incubation using Cytation 3 imaging reader (BioTek, Sursee,
575 Switzerland) at Ex/Em 485/520 nm.

576 ***Ex vivo organotypic cerebellum slice culture (OCSC)***

577 Cerebellar slices were prepared from P8-10 C57BL/6JRj mouse pups as described in[38]. Briefly, Wild
578 type C57BL/6JRj mice pups were sacrificed at postnatal day (PND) 8–10 by decapitation. Cerebella
579 were dissected and kept in ice-cold Geys balanced salt solution containing kynurenic acid (GBSSK) and
580 then embedded in 2% low melting point agarose gel. Solidified agarose blocks were glued onto the
581 vibratome (VT 1200S, Leica, Wetzlar, Germany), and 350 µm thick sections were cut. Slices were
582 transferred on inserts (PICM 03050, Merck Millipore, Burlington, VT, USA) for further *in vitro* culture and

583 were kept in culture for 15 days. Medium was changed daily, and cultures were monitored for signs of
584 cell death. Tumor spheroids were formed from 2500 DAOY LA-EGFP or HD-MBO3 LA-EGFP cells
585 seeded in ultra-low adhesion plate for 48 h before implantation on OCSCs. Just before implantation,
586 spheroid size and integrity were evaluated under the microscope to confirm viability, integrity, and similar
587 spheroid size among the different conditions. The slice-spheroid co-cultures were treated with EGF (30
588 ng/ml), bFGF (12.5 ng/ml), PKCθ inhibitor (5 μM) or Rottlerin (5 μM) for 5 days where indicated. For
589 experiments with siRNA transfected cells, the cells were re-seeded to form spheroids in ultra-low
590 adhesion plate, implanted on the slices 48 h after transfection, and then grown on the slices for other
591 48 h with or without GF treatment. Following the treatment, the co-cultures were fixed with 4%
592 paraformaldehyde and stained for calbindin, GFAP, or anti-human nuclei, and analyzed using IFA as
593 described in[38]. To evaluate the extent of proliferation both in the tumor cells and in the slice culture,
594 we performed 5-ethynyl-2′-deoxyuridine (EdU) staining using the Click-iT EdU Alexa Fluor 647 imaging
595 kit (C10340, Invitrogen). Four-color image acquisition of three replicates per condition was performed
596 on an SP8 confocal microscope (Leica). The area of the infiltrating spheroids and the number of EdU-
597 positive nuclei were measured with ImageJ (Fiji)[72] using the tool analyzed particles after adjusting the
598 threshold to the same value for all the compared conditions.

599 ***In vitro VASP kinase assay***

600 2 x 10^6 DAOY cells expressing FLAG-tagged MAP4K4 were transfected with siCTRL or siSTRN3 as
601 described above. 48 h after the transfection and O/N starvation, cells were stimulated with 100 ng/ml
602 bFGF for 15 minutes and lysed at 4°C with 400 μl of buffer containing 50 mM Tris-HCl (pH 7.5), 150 nM
603 NaCl, 0.3% NP-40 supplemented with protease and phosphatase inhibitors. Parental WT DAOY cells
604 were used as a negative control. Lysates were cleared by centrifugation, and protein concentrations
605 were normalized among the samples. The supernatants were immune precipitated with 30 μl of
606 Dynabeads Protein G magnetic beads (10004D, Thermo Fisher Scientific) coated with anti-FLAG
607 monoclonal antibody (F1804, Sigma) for 3 h at 4°C. The beads were washed twice in lysis buffer and
608 twice with kinase assay buffer (20 mM Tris [pH 7.4], 200 mM NaCl, 0.5 mM dithiothreitol, 10 mM MgCl2).
609 The washed beads were resuspended in 25 μl of kinase assay buffer with 100 μM ATP (A7699, Sigma)
610 supplemented with phosphatase inhibitors and incubated for 20 min in an Eppendorf Thermomixer at
611 30°C at maximal mixing velocity. Then 4 μg of recombinant human VASP protein (ab105601, Abcam)
612 was added, and the reactions were allowed to continue for 10 min at 30°C. The kinase reactions were

613 stopped by adding Laemmli Sample Buffer (1610747, Bio-Rad) containing 50 mM DTT and boiling the
614 samples at 95°C for 5 min. The beads were then magnetically separated from the supernatant, and the
615 samples were analyzed by IB as described above.

616 ***Patient gene expression and proteomic data***

617 Gene expression and proteomic data of pediatric brain tumor patients were obtained from the ProTrack
618 data portal (http://pbt.cptac-data-view.org/) from the Clinical Proteomic Tumor Analysis Consortium
619 (CPTAC) and the Children's Brain Tumor Tissue Consortium (CBTTC). The dataset used includes a
620 cohort of 218 tumor samples representing seven distinct histological diagnoses, including
621 medulloblastoma (MB), low-grade glioma (LGG), high-grade glioma (HGG), ependymoma (EP),
622 craniopharyngioma (CP), ganglioglioma (GG), and atypical teratoid rhabdoid tumor (ATRT)[32].

623 ***Protein kinase activity profiling***

624 4.5 x 10^5 DAOY cells were transfected with siRNA as described above. 72 h after the transfection and
625 O/N starvation, cells were stimulated with 100 ng/ml bFGF for 15 minutes and lysed in M-PER protein
626 extraction reagent (Thermo Fischer Scientific) supplemented with Halt Phosphatase Inhibitor Cocktail
627 and Halt Protease Inhibitor Cocktail EDTA free (Thermo Fischer Scientific). Lysates were cleared by
628 centrifugation, and protein concentrations were determined by Pierce BCA Protein Assay Kit (Thermo
629 Fisher Scientific). Aliquots of 1 mg/ml of lysates were prepared and snap-frozen in liquid nitrogen. Kinase
630 activity profiles were performed using the PamChip® serine/threonine (STK) and protein tyrosine (PTK)
631 peptide microarray system from PamGene ('s-Hertogenbosch, The Netherlands), according to standard
632 manufacturer's instructions. The PamChip® consists of 4 identical peptide arrays, each array containing
633 144 (STK) or 196 (PTK) peptides. The technology measures the phosphorylation of the arrayed STK
634 and PTK peptides and compares derived peptide phosphorylation signatures to known consensus
635 signatures of kinases to predict kinase activities. Three PamChip® microarrays were processed at the
636 same time on the PamStation®12 (PamGene). One and five µg of protein extract were used for the STK
637 array and the PTK array protocol, respectively, and the enzymatic assay was started by adding ATP
638 (final concentration 100 µM). For the PTK array, fluorescein isothiocyanate (FITC)–labeled pY20
639 antibody was incubated on the chip, and the phosphorylation of the individual Tyr peptides was followed
640 by fluorescence detection in real-time. For the STK array, the primary antibody mixture was incubated

641 with the chip, and the secondary FITC- conjugated antibody was used to quantify the signal. For each
642 condition, three biological replicates were performed and analyzed in three different runs.

643 ***Software and data analysis***

644 The fluorescent signal intensity for each peptide on the PamChip® was quantitated by BioNavigator
645 software (PamGene) and represented as linear regression slope as a function of exposure time. A local
646 background correction was used per spot. Nominal CV (Coefficient of variation) was calculated per
647 peptide with a 2-component error fit model, using the overall mean as input. Only peptides that showed
648 nominal CV <0.5 were included in the analysis. Additionally, Combat correction/normalization was
649 performed to correct for differences in batch effects. After averaging signal intensities across the 3
650 biological replicates per condition, the signal ratio between siTarget and siCTRL was used to calculate
651 fold change (FC) values. Peptides with a FC > 1.67 or FC < 0.6 were considered differentially
652 phosphorylated. To generate the peptide phosphorylation heatmap and compare the global
653 phosphorylation levels, the linear regression slope of each peptide was $\log_2$ transformed. Peptides
654 differently phosphorylated in siTarget vs. siCTRL were identified by ANOVA and postHoc Dunnett's
655 tests. Venn diagram analyses were performed in Venny 2.1 (https://bioinfogp.cnb.csic.es/tools/venny/).
656 An upstream kinase prediction tool based on the PamApp on BioNavigator Analysis software was used
657 to generate a putative list of kinases responsible for phosphorylating the phosphosites on the PamChip.
658 The prediction of the differentially activated upstream kinases for each experimental group (siTarget vs.
659 siCTRL, or bFGF vs. UT) is carried out by a comparison of the phosphorylation sites of the peptides on
660 the array with databases containing experimental and literature-based protein modifications such as
661 HPRD, PhosphoELM (http://phospho.elm.eu.org), PhosphoSite Plus (https://www.phosphosite.org),
662 Reactome (http://reactome.org), UNIPROT (https://www.uniprot.org/) and in silico computational
663 predictions database such as PhosphoNet (http://www.phosphonet.ca/). The prediction tool functional
664 rank-orders the top kinases differentially activated between two compared groups. The mean kinase
665 statistic represents the difference in the predicted protein kinase activity between the two compared
666 groups. A positive value indicates an activation, while a negative value an inhibition. The specificity
667 score indicates the specificity of the normalized kinase statistics with respect to the number of peptides
668 used for predicting the corresponding kinase. The higher the specificity score, the higher is the power
669 of the prediction. Values of the specificity score >0.9 were considered as statistically relevant. To group

670 the kinases into sequence families, phylogenetic trees were created using the web-based kinome tool
671 CORAL (http://phanstiel-lab.med.unc.edu/CORAL/).

672 ***Statistical analysis***

673 Statistical analyses were performed using GraphPad Prism 8 software (San Diego, California).
674 Statistical significance of differences between groups was determined using Student's *t*-test (unpaired,
675 two-tailed) or one-way ANOVA repeated-measures test with Bonferroni's correction. The experiments
676 were performed in at least three independent biological replicates (n=3) unless differently indicated, and
677 results are shown as mean ± standard deviation (SD) or standard error of the mean (SEM). The results
678 were considered significant when $p < 0.05$ (*$p \leq 0.05$, ** $p \leq 0.01$, *** $p \leq 0.001$, **** $p \leq 0.0001$). Where
679 indicated, asterisks show statistical significances between control and test sample.

680 ## References

681 1. Hatten, M. E. & Roussel, M. F. (2011) Development and cancer of the cerebellum. *Trends*
682 *Neurosci.* **34**, 134–142.

683 2. Cavalli, F. M. G. *et al.* (2017) Intertumoral Heterogeneity within Medulloblastoma Subgroups.
684 *Cancer Cell* **31**, 737--754.e6.

685 3. Schwalbe, E. C., Lindsey, J. C., Nakjang, S., Crosier, S., Smith, A. J., Hicks, D., Rafiee, G., Hill,
686 R. M., Iliasova, A., Stone, T., Pizer, B., Michalski, A., Joshi, A., Wharton, S. B., Jacques, T. S.,
687 Bailey, S., Williamson, D. & Clifford, S. C. (2017) Novel molecular subgroups for clinical
688 classification and outcome prediction in childhood medulloblastoma: a cohort study. *Lancet*
689 *Oncol.* **18**, 958–971.

690 4. Hovestadt, V., Ayrault, O., Swartling, F. J., Robinson, G. W., Pfister, S. M. & Northcott, P. A.
691 (2020) Medulloblastomics revisited: biological and clinical insights from thousands of patients.
692 *Nat. Rev. Cancer* **20**, 42–56.

693 5. Wu, X. *et al.* (2012) Clonal selection drives genetic divergence of metastatic medulloblastoma.
694 *Nature* **482**, 529–533.

695 6. Santhana Kumar, K., Neve, A., Guerreiro Stucklin, A. S., Kuzan-Fischer, C. M., Rushing, E. J.,
696 Taylor, M. D., Tripolitsioti, D., Behrmann, L., Kirschenbaum, D., Grotzer, M. A. & Baumgartner,

697 M. (2018) TGF-β Determines the Pro-migratory Potential of bFGF Signaling in Medulloblastoma.
698 *Cell Rep.* **23**, 3798-3812.e8.

699 7. Neve, A., Migliavacca, J., Capdeville, C., Schönholzer, M. T., Gries, A., Ma, M., Kumar, K. S.,
700 Grotzer, M. & Baumgartner, M. (2019) Crosstalk between SHH and FGFR signaling pathways
701 controls tissue invasion in medulloblastoma. *Cancers (Basel).* **11**, 1985.

702 8. Juraschka, K. & Taylor, M. D. (2019) Medulloblastoma in the age of molecular subgroups: A
703 review. *J. Neurosurg. Pediatr.* **24**, 353–363.

704 9. Santhana Kumar, K., Tripolitsioti, D., Ma, M., Grählert, J., Egli, K. B., Fiaschetti, G., Shalaby, T.,
705 Grotzer, M. A. & Baumgartner, M. (2015) The Ser/Thr kinase MAP4K4 drives c-Met-induced
706 motility and invasiveness in a cell-based model of SHH medulloblastoma. *Springerplus* **4**, 19.

707 10. Tripolitsioti, D., Kumar, K. S., Neve, A., Migliavacca, J., Capdeville, C., Rushing, E. J., Ma, M.,
708 Kijima, N., Sharma, A., Pruschy, M., McComb, S., Taylor, M. D., Grotzer, M. A. & Baumgartner,
709 M. (2018) MAP4K4 controlled integrin β1 activation and c-Met endocytosis are associated with
710 invasive behavior of medulloblastoma cells. *Oncotarget* **9**, 23220–23236.

711 11. Tripolitsioti, D., Grotzer, M. A. & Baumgartner, M. (2017) The Ser/Thr Kinase MAP4K4 Controls
712 Pro-Metastatic Cell Functions. *J. Carcinog. Mutagen.* **08**, 1–8.

713 12. Flach, R. J. R., Skoura, A., Matevossian, A., Danai, L. V, Zheng, W., Cortes, C., Bhattacharya,
714 S. K., Aouadi, M., Hagan, N., Yawe, J. C., Vangala, P., Menendez, L. G., Cooper, M. P.,
715 Fitzgibbons, T. P., Buckbinder, L. & Czech, M. P. (2015) Endothelial protein kinase MAP4K4
716 promotes vascular inflammation and atherosclerosis. *Nat. Commun.* **6**, 8995.

717 13. Danai, L. V, Roth Flach, R. J., Virbasius, J. V, Garcia Menendez, L., Jung, D. Y., Kim, J. H., Kim,
718 J. K. & Czech, M. P. (2015) Inducible Deletion of Protein Kinase Map4k4 in Obese Mice Improves
719 Insulin Sensitivity in Liver and Adipose Tissues. *Mol. Cell. Biol.* **35**, 2356–2365.

720 14. Collins, C. S., Hong, J., Sapinoso, L., Zhou, Y., Liu, Z., Micklash, K., Schultz, P. G. & Hampton,
721 G. M. (2006) A small interfering RNA screen for modulators of tumor cell motility identifies
722 MAP4K4 as a promigratory kinase. *Proc. Natl. Acad. Sci.* **103**, 3775–3780.

723 15. Prolo, L. M., Li, A., Owen, S. F., Parker, J. J., Foshay, K., Nitta, R. T., Morgens, D. W., Bolin, S.,
724 Wilson, C. M., L, J. C. M. V., Luo, E. J., Nwagbo, G., Waziri, A., Li, G., Reimer, R. J., Bassik, M.

725 C. & Grant, G. A. (2019) Targeted genomic CRISPR-Cas9 screen identifies MAP4K4 as
726 essential for glioblastoma invasion. *Sci. Rep.* **9**, 1420.

727 16. Vitorino, P., Yeung, S., Crow, A., Bakke, J., Smyczek, T., West, K., Mcnamara, E., Eastham-
728 anderson, J., Gould, S., Harris, S. F., Ndubaku, C. & Ye, W. (2015) MAP4K4 regulates integrin-
729 FERM binding to control endothelial cell motility. *Nature* **519**, 425–430.

730 17. Baumgartner, M., Sillman, A. L., Blackwood, E. M., Srivastava, J., Madson, N., Schilling, J. W.,
731 Wright, J. H. & Barber, D. L. (2006) The Nck-interacting kinase phosphorylates ERM proteins for
732 formation of lamellipodium by growth factors. *Proc. Natl. Acad. Sci. U. S. A.* **103**, 13391–13396.

733 18. LeClaire, L. L., Rana, M., Baumgartner, M. & Barber, D. L. (2015) The Nck-interacting kinase
734 NIK increases Arp2/3 complex activity by phosphorylating the Arp2 subunit. *J. Cell Biol.* **208**,
735 161–170.

736 19. Hyodo, T., Ito, S., Hasegawa, H., Asano, E., Maeda, M., Urano, T., Takahashi, M., Hamaguchi,
737 M. & Senga, T. (2012) Misshapen-like kinase 1 (MINK1) is a novel component of striatin-
738 interacting phosphatase and kinase (STRIPAK) and is required for the completion of cytokinesis.
739 *J. Biol. Chem.* **287**, 25019–25029.

740 20. Seo, G., Han, H., Vargas, R. E., Yang, B., Li, X. & Wang, W. (2020) MAP4K Interactome Reveals
741 STRN4 as a Key STRIPAK Complex Component in Hippo Pathway Regulation. *Cell Rep.* **32**,
742 107860.

743 21. Kim, J. W., Berrios, C., Kim, M., Schade, A. E., Adelmant, G., Yeerna, H., Damato, E., Iniguez,
744 A. B., Florens, L., Washburn, M. P., Stegmaier, K., Gray, N. S., Tamayo, P., Gjoerup, O., Marto,
745 J. A., DeCaprio, J. & Hahn, W. C. (2020) STRIPAK directs PP2A activity toward MAP4K4 to
746 promote oncogenic transformation of human cells. *Elife* **9**, 1–27.

747 22. Goudreault, M. *et al.* (2009) A PP2A Phosphatase High Density Interaction Network Identifies a
748 Novel Striatin-interacting Phosphatase and Kinase Complex Linked to the Cerebral Cavernous
749 Malformation 3. *Mol. Cell. proteomics* **8**, 157–171.

750 23. Chen, C., Shi, Z., Zhang, W., Chen, M., He, F., Zhang, Z., Wang, Y., Feng, M., Wang, W., Zhao,
751 Y., Brown, J. H., Jiao, S. & Zhou, Z. (2014) Striatins Contain a Noncanonical Coiled Coil That
752 Binds Protein Phosphatase 2A A Subunit to Form a 2 : 2 Heterotetrameric Core of Striatin-

753 interacting Phosphatase and Kinase (STRIPAK) Complex *. *J. Biol. Chem.* **289**, 9651–9661.

754 24. Kück, U., Radchenko, D. & Teichert, I. (2019) STRIPAK , a highly conserved signaling complex
755 , controls multiple eukaryotic cellular and developmental processes and is linked with human
756 diseases Discovery of striatin. *Biol. Chem.* **400**, 1–18.

757 25. Couzens, A. L., Knight, J. D. R., Kean, M. J., Teo, G., Weiss, A., Dunham, W. H., Lin, Z. Y.,
758 Bagshaw, R. D., Sicheri, F., Pawson, T., Wrana, J. L., Choi, H. & Gingras, A. C. (2013) Protein
759 interaction network of the mammalian hippo pathway reveals mechanisms of kinase-
760 phosphatase interactions. *Sci. Signal.* **6**, rs15.

761 26. Wong, M., Hyodo, T., Asano, E., Funasaka, K., Miyahara, R., Hirooka, Y., Goto, H., Hamaguchi,
762 M. & Senga, T. (2014) Silencing of STRN4 suppresses the malignant characteristics of cancer
763 cells. *Cancer Sci.* **105**, 1526–1532.

764 27. Kim, D. I., Jensen, S. C., Noble, K. A., KC, B., Roux, K. H., Motamedchaboki, K. & Roux, K. J.
765 (2016) An improved smaller biotin ligase for BioID proximity labeling. *Mol. Biol. Cell* **27**, 1188–
766 1196.

767 28. Kim, D. I., Kc, B., Zhu, W., Motamedchaboki, K., Doye, V. & Roux, K. J. (2014) Probing nuclear
768 pore complex architecture with proximity-dependent biotinylation. *Proc. Natl. Acad. Sci.* **111**,
769 E2453-61.

770 29. Roux, K. J., Kim, D. I., Raida, M. & Burke, B. (2012) A promiscuous biotin ligase fusion protein
771 identifies proximal and interacting proteins in mammalian cells. *J. Cell Biol.* **196**, 801–810.

772 30. Kim, J. W. *et al.* (2020) STRIPAK directs PP2A activity toward MAP4K4 to promote oncogenic
773 transformation of human cells. *Elife* **9**, 1–27.

774 31. Tang, Y., Chen, M., Zhou, L., Ma, J., Li, Y., Zhang, H., Shi, Z., Xu, Q., Zhang, X., Gao, Z., Zhao,
775 Y., Cheng, Y., Jiao, S. & Zhou, Z. (2019) Architecture, substructures, and dynamic assembly of
776 STRIPAK complexes in Hippo signaling. *Cell Discov.* **5**, 3.

777 32. Petralia, F. *et al.* (2020) Integrated Proteogenomic Characterization across Major Histological
778 Types of Pediatric Brain Cancer. *Cell* **183**, 1962-1985.e31.

779 33. Kumar, K. S., Pillong, M., Kunze, J., Burghardt, I., Weller, M., Grotzer, M. A., Schneider, G. &
780 Baumgartner, M. (2015) Computer-assisted quantification of motile and invasive capabilities of

781 cancer cells. *Sci. Rep.* **5**, 15338.

782 34. Gordon, J., Hwang, J., Carrier, K. J., Jones, C. A., Kern, Q. L., Moreno, C. S., Karas, R. H. &
783 Pallas, D. C. (2011) Protein phosphatase 2a (PP2A) binds within the oligomerization domain of
784 striatin and regulates the phosphorylation and activation of the mammalian Ste20-Like kinase
785 Mst3. *BMC Biochem.* **12**, 1–18.

786 35. Zheng, Y., Liu, B., Wang, L., Lei, H., Pulgar Prieto, K. D. & Pan, D. (2017) Homeostatic Control
787 of Hpo/MST Kinase Activity through Autophosphorylation-Dependent Recruitment of the
788 STRIPAK PP2A Phosphatase Complex. *Cell Rep.* **21**, 3612–3623.

789 36. Ho, W. S., Feldman, M. J., Maric, D., Amable, L., Matthew, D., Feldman, G. M., Ray-chaudhury,
790 A., Lizak, M. J., Robison, R. A., Zhuang, Z. & Heiss, J. D. (2016) PP2A inhibition with LB100
791 enhances cisplatin cytotoxicity and overcomes cisplatin resistance in medulloblastoma cells.
792 *Oncotarget* **7**, 12447–12463.

793 37. Yang, D., Okamura, H., Morimoto, H., Teramachi, J. & Haneji, T. (2016) Protein phosphatase 2A
794 C $α$ regulates proliferation , migration , and metastasis of osteosarcoma cells. *Lab. Investig.*
795 **96**, 1050–1062.

796 38. Neve, A., Kumar, K. S., Tripolitsioti, D., Grotzer, M. A. & Baumgartner, M. (2017) Investigation
797 of brain tissue infiltration by medulloblastoma cells in an ex vivo model. *Sci. Rep.* **7**, 1–12.

798 39. Meng, Z., Moroishi, T., Mottier-Pavie, V., Plouffe, S. W., Hansen, C. G., Hong, A. W., Park, H.
799 W., Mo, J. S., Lu, W., Lu, S., Flores, F., Yu, F. X., Halder, G. & Guan, K. L. (2015) MAP4K family
800 kinases act in parallel to MST1/2 to activate LATS1/2 in the Hippo pathway. *Nat. Commun.* **6**, 1–
801 13.

802 40. Zheng, Y., Wang, W., Liu, B., Deng, H., Uster, E. & Pan, D. (2015) Identification of
803 Happyhour/MAP4K as Alternative Hpo/Mst-like Kinases in the Hippo Kinase Cascade. *Dev. Cell*
804 **34**, 642–655.

805 41. Ribeiro, P. S., Josué, F., Wepf, A., Wehr, M. C., Rinner, O., Kelly, G., Tapon, N. & Gstaiger, M.
806 (2010) Combined Functional Genomic and Proteomic Approaches Identify a PP2A Complex as
807 a Negative Regulator of Hippo Signaling. *Mol. Cell* **39**, 521–534.

808 42. Chen, R., Xie, R., Meng, Z., Ma, S. & Guan, K. L. (2019) STRIPAK integrates upstream signals

809 to initiate the Hippo kinase cascade. *Nat. Cell Biol.* **21**, 1565–1577.

810 43. Bae, S. J., Ni, L., Osinski, A., Tomchick, D. R., Brautigam, C. A. & Luo, X. (2017) SAV1 promotes
811 Hippo kinase activation through antagonizing the PP2A phosphatase STRIPAK. *Elife* **6**, 1–28.

812 44. Liu, Y., Graham, C., Li, A., Fisher, R. J. & Shaw, S. (2002) Phosphorylation of the protein kinase
813 C-theta activation loop and hydrophobic motif regulates its kinase activity, but only activation
814 loop phosphorylation is critical to in vivo nuclear-factor-κB induction. *Biochem. J.* **361**, 255–265.

815 45. Cywin, C. L. *et al.* (2007) Discovery of potent and selective PKC-θ inhibitors. *Bioorganic Med.*
816 *Chem. Lett.* **17**, 225–230.

817 46. Frey, C. R., Wagle, M.-C., Vaidya, K., Hambleton, J., Lackner, M. & Mounir, Z. (2020) Analysis
818 of drug combinations with the PKC inhibitor IDE196 support dual MEK and PKC inhibition as a
819 rational combination in metastatic uveal melanoma. *Cancer Res.* **80**, 5337 LP – 5337.

820 47. Gschwendt, M., Müller, H. J., Kielbassa, K., Zang, R., Kittstein, W., Rincke, G. & Marks, F. (1994)
821 Rottlerin, a novel protein kinase inhibitor. *Biochemical and Biophysical Research*
822 *Communications* **199**, 93–98.

823 48. Mohammadi, M., Honegger, A. M., Rotin, D., Fischer, R., Bellot, F., Li, W., Dionne, C. A., Jaye,
824 M., Rubinstein, M. & Schlessinger, J. (1991) A tyrosine-phosphorylated carboxy-terminal peptide
825 of the fibroblast growth factor receptor (Flg) is a binding site for the SH2 domain of phospholipase
826 C-gamma 1. *Mol. Cell. Biol.* **11**, 5068–5078.

827 49. Chen, R., Kim, O., Yang, J., Sato, K., Eisenmann, K. M., McCarthy, J., Chen, H. & Qiu, Y. (2001)
828 Regulation of Akt/PKB Activation by Tyrosine Phosphorylation. *J. Biol. Chem.* **276**, 31858–
829 31862.

830 50. Skoble, J., Auerbuch, V., Goley, E. D., Welch, M. D. & Portnoy, D. A. (2001) Pivotal role of VASP
831 in Arp2/3 complex-mediated actin nucleation, actin branch-formation, and Listeria
832 monocytogenes motility. *J. Cell Biol.* **155**, 89–100.

833 51. Barzik, M., Kotova, T. I., Higgs, H. N., Hazelwood, L., Hanein, D., Gertler, F. B. & Schafer, D. A.
834 (2005) Ena/VASP proteins enhance actin polymerization in the presence of barbed end capping
835 proteins. *J. Biol. Chem.* **280**, 28653–28662.

836 52. Benz, P. M., Blume, C., Seifert, S., Wilhelm, S., Waschke, J., Schuh, K., Gertler, F., Münzel, T.

837 & Renné, T. (2009) Differential VASP phosphorylation controls remodeling of the actin
838 cytoskeleton. *J. Cell Sci.* **122**, 3954–3965.

839 53. Harbeck, B., Hüttelmaier, S., Schlüter, K., Jockusch, B. M. & Illenberger, S. (2000)
840 Phosphorylation of the vasodilator-stimulated phosphoprotein regulates its interaction witn actin.
841 *J. Biol. Chem.* **275**, 30817–30825.

842 54. Tang, Y. *et al.* (2020) Selective Inhibition of STRN3-Containing PP2A Phosphatase Restores
843 Hippo Tumor-Suppressor Activity in Gastric Cancer Article Selective Inhibition of STRN3-
844 Containing PP2A Phosphatase Restores Hippo Tumor-Suppressor Activity in Gastric Cancer.
845 *Cancer Cell* **38**, 115-128.e9.

846 55. Garg, R., Benedetti, L. G., Abera, M. B., Wang, H., Abba, M. & Kazanietz, M. G. (2014) Protein
847 kinase C and cancer: What we know and what we do not. *Oncogene* **33**, 5225–5237.

848 56. Du, Q. Y., Yao, J. H., Zhou, Y. C., Xu, L. J., Zhao, F. Y. & Yang, Y. (2020) High STRN Expression
849 Promotes HCC Invasion and Migration but Not Cell Proliferation or Apoptosis through Facilitating
850 Epithelial-Mesenchymal Transition. *Biomed Res. Int.* **2020**, 6152925.

851 57. Lee, T. H., Chen, J. L., Liu, P. S., Tsai, M. M., Tsai, M. M., Wang, S. J., Hsieh, H. L. & Hsieh, H.
852 L. (2020) Rottlerin, a natural polyphenol compound, inhibits upregulation of matrix
853 metalloproteinase-9 and brain astrocytic migration by reducing PKC-$δ$-dependent ROS signal.
854 *J. Neuroinflammation* **17**, 1–13.

855 58. Sarkar, S. & Yong, V. W. (2010) Reduction of protein kinase C delta attenuates tenascin-C
856 stimulated glioma invasion in three-dimensional matrix. *Carcinogenesis* **31**, 311–317.

857 59. Brenner, W., Greber, I., Gudejko-Thiel, J., Beitz, S., Schneider, E., Walenta, S., Peters, K.,
858 Unger, R. & Thüroff, J. W. (2008) Migration of renal carcinoma cells is dependent on protein
859 kinase Cδ via β1 integrin and focal adhesion kinase. *Int. J. Oncol.* **32**, 1125–1131.

860 60. Cannon, J. L., Asperti-Boursin, F., Letendre, K. A., Brown, I. K., Korzekwa, K. E., Blaine, K. M.,
861 Oruganti, S. R., Sperling, A. I. & Moses, M. E. (2013) PKCθ regulates T cell motility via ezrin-
862 radixin-moesin localization to the uropod. *PLoS One* **8**, e78940.

863 61. Madaro, L., Marrocco, V., Fiore, P., Aulino, P., Smeriglio, P., Adamo, S., Molinaro, M. & Bouché,
864 M. (2011) PKCθ signaling is required for myoblast fusion by regulating the expression of

865 caveolin-3 and β1D integrin upstream focal adhesion kinase. *Mol. Biol. Cell* **22**, 1409–1419.

866 62. Parker, P. J. & Murray-Rust, J. (2004) PKC at a glance. *J. Cell Sci.* **117**, 131–132.

867 63. Döppler, H. & Storz, P. (2013) Regulation of VASP by phosphorylation Consequences for cell
868 migration. *Cell Adhes. Migr.* **7**, 482–486.

869 64. Madsen, C. D., Hooper, S., Tozluoglu, M., Bruckbauer, A., Fletcher, G., Erler, J. T., Bates, P. A.,
870 Thompson, B. & Sahai, E. (2015) STRIPAK components determine mode of cancer cell migration
871 and metastasis. *Nat. Cell Biol.* **17**, 68–80.

872 65. Schönholzer, M. T., Migliavacca, J., Alvarez, E., Santhana Kumar, K., Neve, A., Gries, A., Ma,
873 M., Grotzer, M. A. & Baumgartner, M. (2020) Real-time sensing of MAPK signaling in
874 medulloblastoma cells reveals cellular evasion mechanism counteracting dasatinib blockade of
875 ERK activation during invasion. *Neoplasia (United States)* **22**, 470–483.

876 66. Tang, Y. *et al.* (2020) Selective Inhibition of STRN3-Containing PP2A Phosphatase Restores
877 Hippo Tumor-Suppressor Activity in Gastric Cancer. *Cancer Cell* **38**, 115-128.e9.

878 67. Ndubaku, C. O. *et al.* (2015) Structure-Based Design of GNE-495, a Potent and Selective
879 MAP4K4 Inhibitor with Efficacy in Retinal Angiogenesis. *ACS Med. Chem. Lett.* **6**, 913–918.

880 68. Zhou, Y., Zhou, B., Pache, L., Chang, M., Khodabakhshi, A. H., Tanaseichuk, O., Benner, C. &
881 Chanda, S. K. (2019) Metascape provides a biologist-oriented resource for the analysis of
882 systems-level datasets. *Nat. Commun.* **10**, 1523.

883 69. Ma, M. & Baumgartner, M. (2014) Intracellular Theileria annulata Promote Invasive Cell Motility
884 through Kinase Regulation of the Host Actin Cytoskeleton. *PLoS Pathog.* **10**, e1004003.

885 70. Stewart, S. A., Dykxhoorn, D. M., Palliser, D., Mizuno, H., Yu, E. Y., An, D. S., Sabatini, D. M.,
886 Chen, I. S. Y., Hahn, W. C., Sharp, P. A., Weinberg, R. A. & Novina, C. D. (2003) Lentivirus-
887 delivered stable gene silencing by RNAi in primary cells. *Rna* **9**, 493–501.

888 71. McComb, S., Aguadé-Gorgorió, J., Harder, L., Marovca, B., Cario, G., Eckert, C., Schrappe, M.,
889 Stanulla, M., Von Stackelberg, A., Bourquin, J. P. & Bornhauser, B. C. (2016) Activation of
890 concurrent apoptosis and necroptosis by SMAC mimetics for the treatment of refractory and
891 relapsed ALL. *Sci. Transl. Med.* **8**, 339ra70.

892 72. Schindelin, J., Arganda-Carreras, I., Frise, E., Kaynig, V., Longair, M., Pietzsch, T., Preibisch,

893 S., Rueden, C., Saalfeld, S., Schmid, B., Tinevez, J. Y., White, D. J., Hartenstein, V., Eliceiri, K.,
894 Tomancak, P. & Cardona, A. (2012) Fiji: An open-source platform for biological-image analysis.
895 *Nat. Methods* **9**, 676–682.

896 73. Jeong, B., Bae, S. J., Ni, L., Zhang, X., Bai, X. & Luo, X. (2021) Cryo-EM structure of the Hippo
897 signaling integrator human STRIPAK. *Nat. Struct. Mol. Biol.* **28**, 290–299.

898

899 Acknowledgments

900 The authors thank Dr. Savithri Rangarajan (PamGene International) for scientific support and analysis
901 of PamChip imaging data and Dr. Jens Sobek (Functional Genomics Center Zurich) for assistance with
902 the experiments performed on PamStation®12. We would like to thank members of the Functional
903 Genomics Center Zurich for mass spectrometry support. Imaging was performed with equipment
904 maintained by the Centre for Microscopy and Image Analysis, University of Zurich. This study was
905 supported by grants from the Swiss National Science foundation (SNF_31003A_165860/1,
906 SNF_310030_188793) and the Swiss Cancer League (SCL_KLS-3834-02-2016) to MB, the University
907 of Zürich (Candoc) to J.M. and from the Childhood Cancer Foundation to MG.

908 Author contributions

909 J.M. contributed to designing the study, planned and conducted all the experiments, prepared the
910 figures, and wrote the manuscript. B.Z. generated DAOY cells stably expressing different MAP4K4
911 domains. C.C. provided experimental support for image acquisition and quantification with the Operetta
912 microscope. M.G. helped to draft the study. M.B. designed and drafted the study and wrote the
913 manuscript.

914

915 Figures

916 **Figure 1: BioID identifies MAP4K4-STRIPAK complex interaction in MB cells. (A)** Gene ontology
917 (GO) classifications of MAP4K4-interacting protein from BioID experiments conducted in HEK-293T.
918 Mass spectrometry was performed after immunoprecipitation (IP) with streptavidin-conjugated beads of
919 N- or C- BioID2-MAP4K4 and BioID2 alone overexpressing cells. **(B)** Volcano-plots of interacting

920 proteins in N-BioID2-MAP4K4 (left) or C-BioID2-MAP4K4 (right) HEK-293T cells compared to BioID2-
921 CTRL. Log_2 ratios of cumulated peptide detection values plotted against negative Log_{10} p-values of
922 Student's *t*-test. Enriched proteins are highlighted in red ($p < 0.05$ and > 2-fold enrichment) and members
923 of the STRIPAK complex indicated. *n*=3. **(C)** Architecture of the STRIPAK complex, adapted from[73].
924 **(D)** Immunoblot (IB) detection of BioID2-MAP4K4-FLAG and components of STRIPAK complex in anti-
925 FLAG-IP HEK-293T cells. **(E)** Volcano-plots of protein interactions identified by streptavidin affinity
926 purification-MS in N-BioID2-MAP4K4 (left) or C-BioID2-MAP4K4 (right) DAOY cells compared to
927 BioID2-CTRL. Members of the STRIPAK complex are highlighted. *n*=2. **(F)** IB of MAP4K4-FLAG and
928 components of STRIPAK complex after anti-FLAG-IP in DAOY cells. **(G)** IB analysis of MAP4K4 and
929 components of STRIPAK complex after anti-STRN4 (top) or anti-STRIP1 (bottom) immunoprecipitation
930 in DAOY cells transfected for 48 h with the indicated siRNA. Normal rabbit IgG was used as control for
931 the IP. **(H)** Top: MAP4K4 domain architecture and MAP4K4 constructs used. Numbers represent the
932 amino acids corresponding to full-length MAP4K4. KD, kinase domain; ID, intermediate domain; CNH,
933 citron homology domain; CC, coiled-coil. Lower: Co-IP and IB analysis of STRN4 and STRIP1 in DAOY
934 cells transduced with lentiviral vectors expressing full-length or truncated MAP4K4-FLAG. Asterisks
935 indicate relevant bands. **(I)** Quantification of co-IP from H (*n*=3, means ± SEM). See also Figure S1.
936
937 **Figure 2: STRIPAK complex disruption impairs GF-induced collagen I invasion. (A)** Invasion and
938 representative images of 3D spheroid invasion assay (SIA) of DAOY cells transfected with 10 nM of the
939 indicated siRNA ± GFs (EGF: 30 ng/ml, bFGF: 100 ng/ml). Invasion is calculated as sum of the distances
940 of each migrating cell from the center of the spheroids (*n*=4, means ± SEM). **(B)** SIA of UW228 cells
941 transfected with 10 nM of the indicated siRNA ± 100 ng/ml bFGF (*n*=4, means ± SEM). **(C)** SIA and
942 representative images of DAOY cells ± 100 ng/ml bFGF and ± increasing concentrations of PP2A
943 inhibitor LB-100 (*n*=3, means ± SEM). * $p < 0.05$, ** $p < 0.01$, *** $p < 0.001$, **** $p < 0.0001$ (one-way
944 ANOVA). See also Figure S3.
945
946 **Figure 3: STRN3 is necessary for invasive growth of SHH and group 3 MB cell model in cerebellar**
947 **tissue. (A**) Maximum intensity projections (MIP) of representative confocal sections of organotypic
948 cerebellum slice culture (OCSCs) implanted with DAOY tumor cell spheroids for 48h. Green: Lifeact-
949 EGFP; blue: calbindin (Purkinje cells); red: GFAP. Middle: Inverted greyscale images of MIP of LA-
950 EGFP channel, lower: Inverted greyscale images of MIP of EdU-Click-IT staining. Scale bar: 200 µm.
951 **(B)** Quantification of LA-EGFP area of DAOY spheroids shown in A (*n*=3, means ± SD). **(C)** OCSCs
952 culture implanted with tumor spheroids derived from HD-MBO3 cells KO for MAP4K4, STRN4, STRN3,
953 or STRIP1. MIP of representative slices five days after implantation and ± treatment with 30 ng/ml EGF
954 or 12.5 ng/ml bFGF. Green: Lifeact-EGFP; blue: calbindin (Purkinje cells); red: GFAP; yellow: Edu-Click-
955 IT. Scale bar: 200 µm. **(D)** Areas of LA-EGFP positive HD-MBO3 spheroids showed in C (*n*=3, means
956 ± SD). **(E)** Number of EdU-positive nuclei normalized by the area in pixels of the tumor spheroids (*n*=3,
957 means ± SD). * $p < 0.05$, ** $p < 0.01$, *** $p < 0.001$, **** $p < 0.0001$ (unpaired Student's *t*-test). See also
958 Figure S4 and S5.
959

960 **Figure 4: STRN3/4 and MAP4K4 display opposing functions towards MB cell proliferation, clonal**
961 **growth and YAP/TAZ target gene expression. (A, B)** Representative images and quantification of
962 colony formation assay of DAOY (A) and HD-MBO3 cells (B) KO for MAP4K4, STRN4, STRN3, or
963 STRIP1 ± 100 ng/ml bFGF (*n*=3, means ± SEM). **(C)** qRT-PCR analysis of YAP/TAZ target genes in
964 DAOY cells 48 h after transfection with siRNAs as indicated. (*n*=4, means ± SEM). **(D)** qRT-PCR
965 analysis of YAP/TAZ target genes in HD-MBO3 with CRISPR/Cas9-mediated knockout of MAP4K4,
966 STRN4, STRN3, or STRIP1 (*n*=3, means ± SEM). **(E)** qRT-PCR analysis of *CTGF* expression in DAOY
967 cells 48 h after transfection with the indicated siRNA ± treatment for 4 h with 5 µM LB-100 (*n*=3, means
968 ± SEM). **(F, G)** qRT-PCR analysis of *CTGF* expression in DAOY (F) or HD-MBO3 cells (G) transfected
969 with siRNA for 48 h, serum-starved overnight, and treated with 100 ng/ml bFGF for 1 h and/or 5 µM LB-
970 100 for 4 h where indicated (*n*=3, means ± SEM). * $p < 0.05$, ** $p < 0.01$, *** $p < 0.001$, **** $p < 0.0001$
971 (unpaired Student's *t*-test). See also Figure S6.
972
973 **Figure 5: Novel protein kinases C are pro-migratory effectors of MAP4K4 and STRN3. (A)** Kinase
974 activity prediction analysis in DAOY cells transfected with the indicated siRNAs and ± stimulation with
975 100 ng/ml bFGF for 15 min. The plots show the predicted top 25 differentially activated serine/threonine
976 kinases (STK). The x-axis indicates differences in the activity of the predicted protein kinase between
977 the two groups, with effect size (values) and direction (>0=activation; <0=inhibition). The color of the
978 bars represents the specificity score (darker to light is higher to lower score). Values >0.9 were
979 considered as statistically relevant. First graph from left: comparison of bFGF stimulated siCTRL cells
980 vs. untreated (UT); all other graphs: comparison of the indicated siTarget vs. siCTRL with bFGF
981 stimulation. Highlighted in red are novel PKC isoforms (δ, ε, η and θ) (*n*=3). **(B)** IB analysis and
982 quantification of PKCθ T_{538} phosphorylation in DAOY cells 72 h after siRNA transfection ± 100 ng/ml
983 bFGF for 15 min (*n*=4, means ± SEM). **(C)** Quantification and representative images of SIA with DAOY
984 cells stimulated with 100 ng/ml bFGF and treated with increasing concentrations of PKCθ inhibitor.
985 Invasion was quantified as the sum of invasion distances from the center of the spheroids. DMSO was
986 used as negative control (*n*=4, means ± SEM). **(D)** Maximum intensity projections (MIP) of
987 representative confocal sections of OCSCs implanted with DAOY tumor cell spheroids and treated with
988 5 µM PKCθ inhibitor or DMSO for five days. Green: Lifeact-EGFP; blue: calbindin (Purkinje cells); red:
989 GFAP; yellow: Edu-Click-IT. Scale bar: 200 µm. **(E)** Quantification of LA-EGFP area of DAOY spheroids
990 shown in D (*n*=3, means ± SD). **(F)** Quantification of number of EdU-positive nuclei normalized by the
991 area of DAOY spheroids shown in D (*n*=3, means ± SD). **(G)** Quantification and representative images
992 of SIA of siCTRL or siPKCθ transfected DAOY cells ± 100 ng/ml bFGF (*n*=4, means ± SEM). **(H)** MIP
993 of representative confocal sections of OCSC implanted with transfected DAOY tumor cell spheroids and
994 treated with 12.5 ng/ml bFGF for 48h. Green: Lifeact-EGFP; blue: calbindin (Purkinje cells); red: GFAP;
995 yellow: Edu-Click-IT. Scale bar: 200 µm. **(I)** Quantification of LA-EGFP area of DAOY spheroids shown
996 in H (*n*=3, means ± SD). Statistical analyses in C and G were performed by one-way ANOVA, in B, E,
997 F and I by unpaired Student's t-test. * $p < 0.05$, ** $p < 0.01$, *** $p < 0.001$, **** $p < 0.0001$. See also
998 Figure S7 and S8.
999

1000 **Figure 6: MAP4K4 and STRN3 mediate VASP$_{S157}$ phosphorylation. (A)** Heat map of increased (red)
1001 and decreased (blue) phosphorylation of Ser/Thr (STK, left) or Tyr (PTK, right) consensus peptides
1002 associated with lysates from siRNA transfected DAOY cells treated ± 100 ng/ml bFGF for 15 min. Log_2
1003 of the fold change between siTarget and siCTRL (*n*=3). **(B)** Venn diagram displaying the number of
1004 Ser/Thr and Tyr peptides with significantly changed phosphorylation ($p < 0.1$) in each siTarget versus
1005 siCTRL with bFGF stimulation (*n*=3). **(C)** Volcano plots representing the changes in phosphorylation of
1006 STK (circles) and PTK (diamonds) peptides in siMAP4K4 (upper) or siSTRN3 (lower) versus siCTRL
1007 with bFGF stimulation. Blue: peptides with significantly decreased (fold change < 0.6), red: peptides with
1008 significantly increased phosphorylation (fold change > 1.67). The p-values were calculated versus
1009 siCTRL by ANOVA and post-hoc Dunnett's test in the BioNavigator software. *n*=3. See also Table S3.
1010 **(D)** Single confocal section of VASP localization in DAOY cells seeded on collagen-coated plates ± 100
1011 ng/ml bFGF for 15 min. 3X magnifications of boxed areas are shown. Red: VASP, Green: Lifeact-EGFP.
1012 Blue: DNA Hoechst. Scale bar: 20 µm. **(E)** IB and quantification of VASP$_{S157}$ phosphorylation in DAOY
1013 cells 72 h after siRNA transfection ± 100 ng/ml bFGF for 15 min (*n*=4, means ± SEM). **(F)** IB and
1014 quantification of VASP$_{S157}$ phosphorylation in DAOY cells expressing full-length or truncated (KD-ID1-
1015 ID2) MAP4K4-FLAG ± 100 ng/ml bFGF for 15 min (*n*=3, means ± SEM). **(G)** In vitro VASP S157
1016 phosphorylation of FLAG-immunoprecipitated DAOY cells expressing FLAG-tagged MAP4K4 and
1017 transfected for 48 h with the indicated siRNA ± 100 ng/ml bFGF for 15 min. The *in vitro* kinase reaction
1018 was conducted incubating the IP fraction with a recombinant VASP protein. Parental WT DAOY cells
1019 were used as a negative control for the IP. **(H)** Quantification and representative images of SIA of
1020 siCTRL or siVASP transfected DAOY cells ± 100 ng/ml bFGF (*n*=4, means ± SEM). Statistical analysis
1021 in E and F was performed by unpaired Student's t-test, in H by one-way ANOVA. * $p < 0.05$, ** $p < 0.01$,
1022 **** $p < 0.0001$. See also Figure S9.
1023
1024 **Figure 7: Proposed model of MAP4K4 and STRN3 regulation of cell migration and proliferation**
1025 **in MB.** MAP4K4 is activated downstream of RTK signaling and exerts both pro-invasive and anti-
1026 proliferative activities in MB cells. Invasion regulation: STRN3 cooperates with MAP4K4 to control cell
1027 migration, invasion, and actin cytoskeleton remodeling, independently from PP2A activity. This
1028 cooperation of MAP4K4 and STRN3 is necessary for the FGFR-induced activation of motility-associated
1029 effectors nPKCs and VASP. Proliferation regulation: MAP4K4 causes LATS1/2 phosphorylation, which
1030 promotes the activation of the Hippo pathway. Hippo pathway activation results in the phosphorylation
1031 and degradation of the transcriptional regulator YAP. The consequent repression of YAP transcriptional
1032 activity leads to a proliferation arrest. STRN3 promotes PP2A-mediated inactivation of MAP4K4 function
1033 toward Hippo activation, resulting in an increase of YAP transcriptional activity and cell proliferation.

Graphical abstract

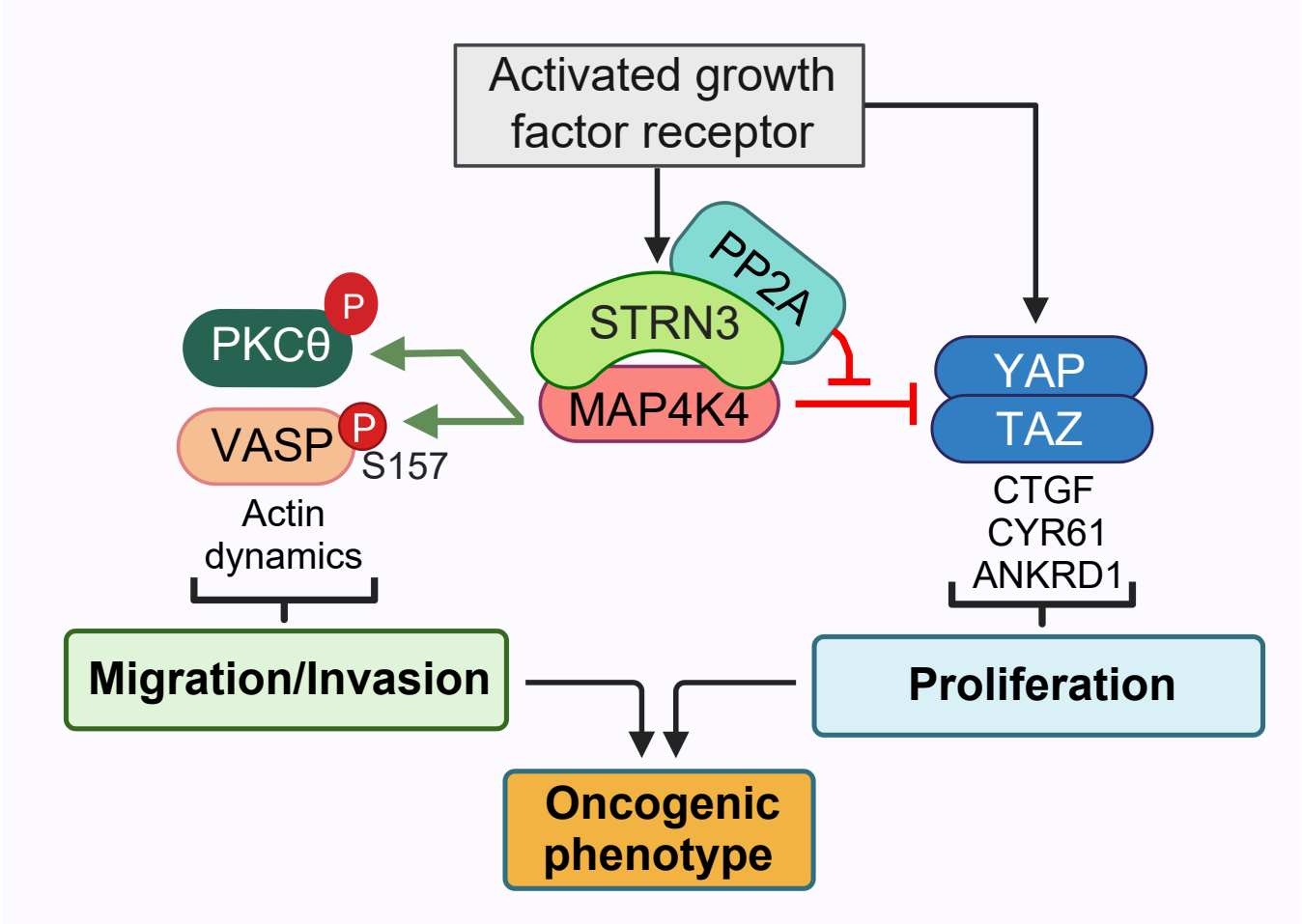

Figure 1

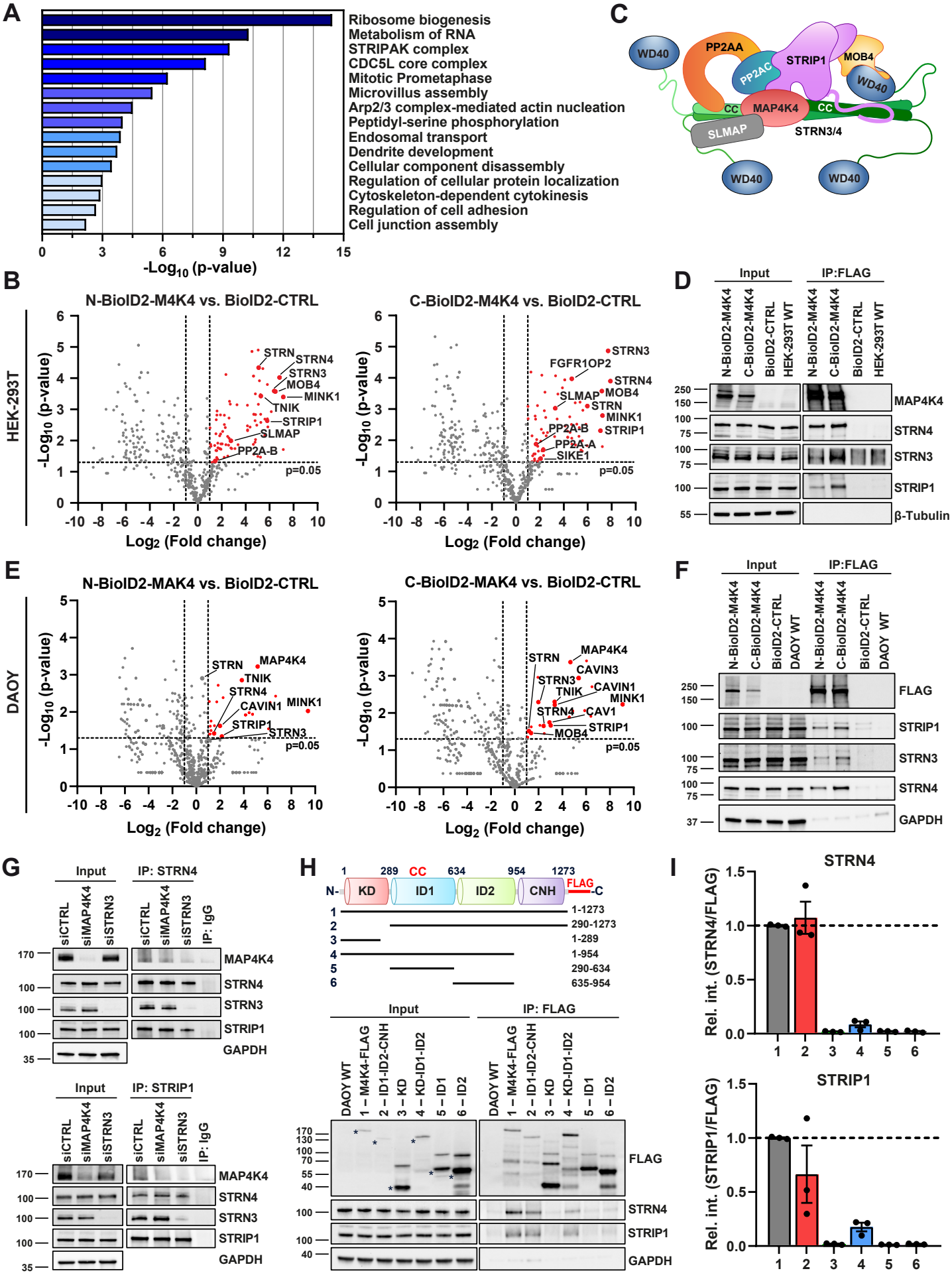
A
Ribosome biogenesis
Metabolism of RNA
STRIPAK complex
CDC5L core complex
Mitotic Prometaphase
Microvillus assembly
Arp2/3 complex-mediated actin nucleation
Peptidyl-serine phosphorylation
Endosomal transport
Dendrite development
Cellular component disassembly
Regulation of cellular protein localization
Cytoskeleton-dependent cytokinesis
Regulation of cell adhesion
Cell junction assembly
-Log10 (p-value)
B
N-BioID2-M4K4 vs. BioID2-CTRL
C-BioID2-M4K4 vs. BioID2-CTRL
HEK-293T
-Log10 (p-value)
Log2 (Fold change)
p=0.05
C
WD40
PP2AA
PP2AC
STRIP1
MOB4
CC
MAP4K4
SLMAP
STRN3/4
D
Input
IP:FLAG
N-BioID2-M4K4
C-BioID2-M4K4
BioID2-CTRL
HEK-293T WT
MAP4K4
STRN4
STRN3
STRIP1
β-Tubulin
E
N-BioID2-MAK4 vs. BioID2-CTRL
C-BioID2-MAK4 vs. BioID2-CTRL
DAOY
F
DAOY WT
FLAG
GAPDH
G
siCTRL
siMAP4K4
siSTRN3
IP: STRN4
IP: STRIP1
IP: IgG
H
KD
ID1
ID2
CNH
FLAG
1-1273
290-1273
1-289
1-954
290-634
635-954
DAOY WT
1 – M4K4-FLAG
2 – ID1-ID2-CNH
3 – KD
4 – KD-ID1-ID2
5 – ID1
6 – ID2
I
STRN4
STRIP1
Rel. int. (STRN4/FLAG)
Rel. int. (STRIP1/FLAG)

Figure 2

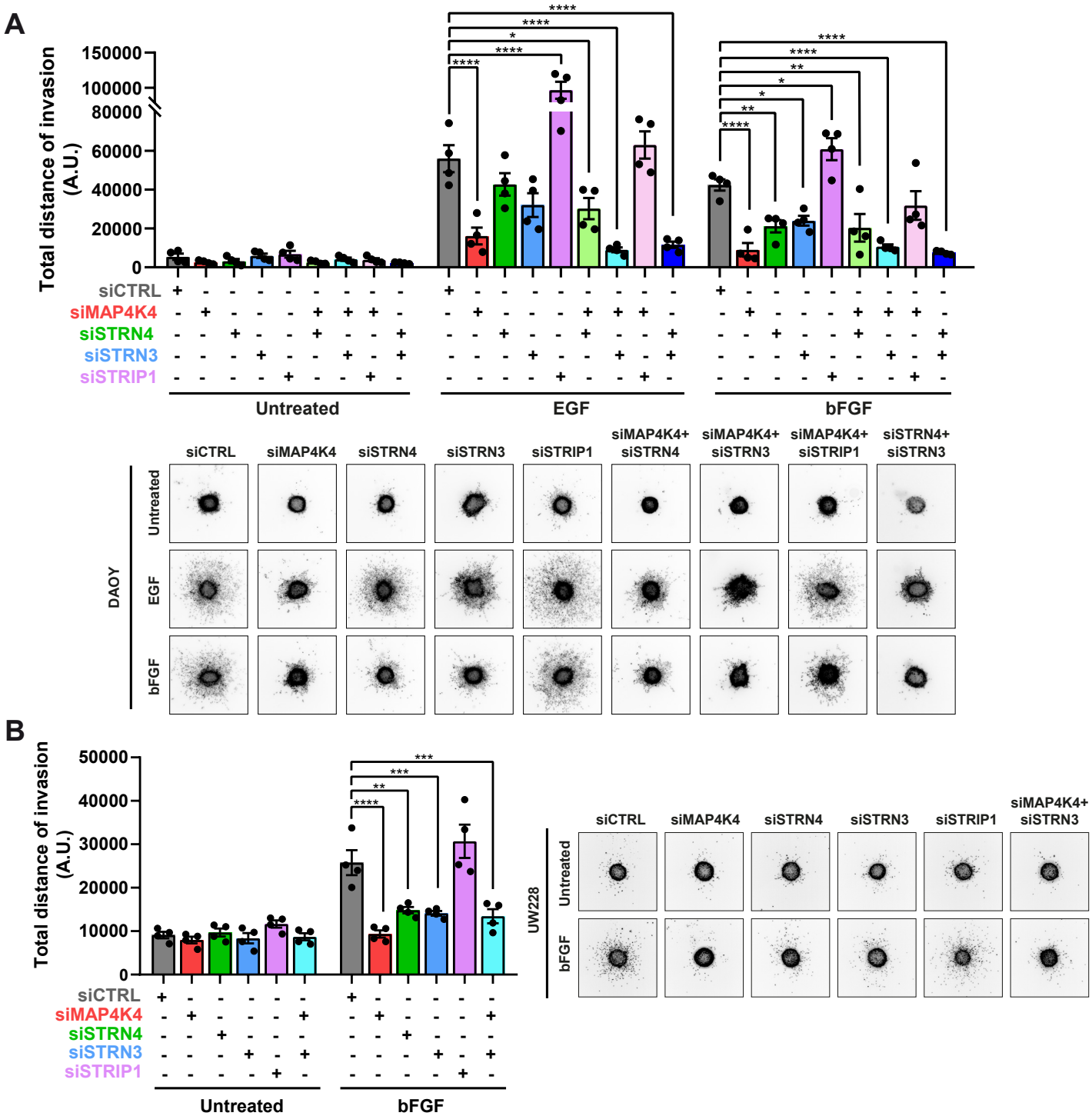
A
Total distance of invasion (A.U.)
150000
100000
80000
60000
40000
20000
0
siCTRL
siMAP4K4
siSTRN4
siSTRN3
siSTRIP1
Untreated
EGF
bFGF
siCTRL
siMAP4K4
siSTRN4
siSTRN3
siSTRIP1
siMAP4K4+ siSTRN4
siMAP4K4+ siSTRN3
siMAP4K4+ siSTRIP1
siSTRN4+ siSTRN3
DAOY
Untreated
EGF
bFGF
B
Total distance of invasion (A.U.)
50000
40000
30000
20000
10000
0
siCTRL
siMAP4K4
siSTRN4
siSTRN3
siSTRIP1
Untreated
bFGF
siCTRL
siMAP4K4
siSTRN4
siSTRN3
siSTRIP1
siMAP4K4+ siSTRN3
UW228
Untreated
bFGF
C
Total distance of invasion (A.U.)
30000
25000
20000
15000
10000
5000
0
bFGF
LB-100 [μM]
0
0.25
0.5
1
2
3
4
5
6
8
10
UT
bFGF
bFGF + 250 nM
bFGF + 500 nM
bFGF + 1 μM
bFGF + 2 μM
bFGF + 3 μM
bFGF + 4 μM
bFGF + 5 μM
bFGF + 6 μM
bFGF + 8 μM
bFGF + 10 μM

Figure 3

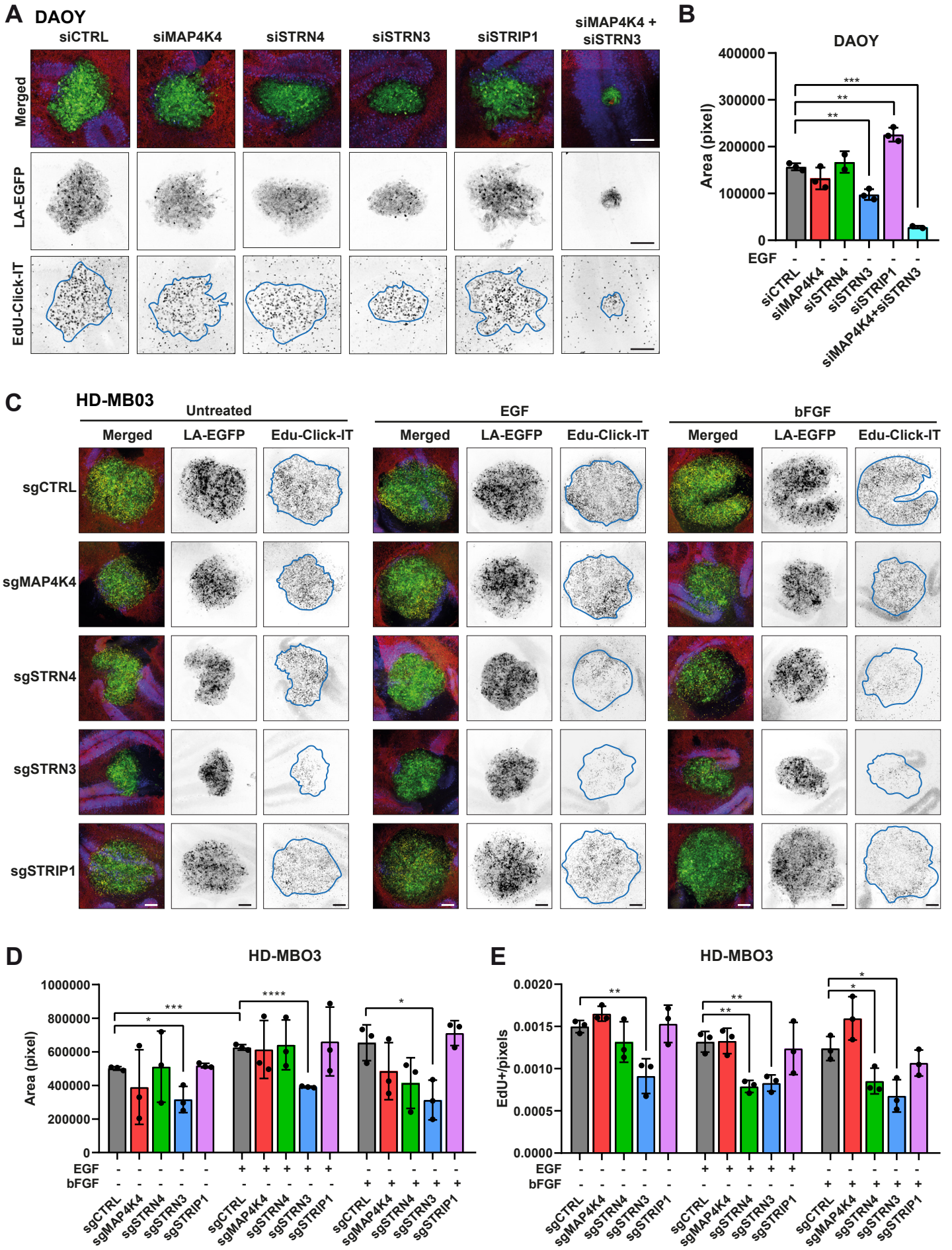
A
DAOY
siCTRL
siMAP4K4
siSTRN4
siSTRN3
siSTRIP1
siMAP4K4 + siSTRN3
Merged
LA-EGFP
EdU-Click-IT
B
DAOY
Area (pixel)
400000
300000
200000
100000
0
***
**
**
EGF
siCTRL
siMAP4K4
siSTRN4
siSTRN3
siSTRIP1
siMAP4K4+siSTRN3
C
HD-MB03
Untreated
EGF
bFGF
Merged
LA-EGFP
Edu-Click-IT
sgCTRL
sgMAP4K4
sgSTRN4
sgSTRN3
sgSTRIP1
D
HD-MBO3
Area (pixel)
1000000
800000
600000
400000
200000
0
***
*
****
*
EGF
bFGF
sgCTRL
sgMAP4K4
sgSTRN4
sgSTRN3
sgSTRIP1
E
HD-MBO3
EdU+/pixels
0.0020
0.0015
0.0010
0.0005
0.0000
**
**
**
*
*
EGF
bFGF
sgCTRL
sgMAP4K4
sgSTRN4
sgSTRN3
sgSTRIP1

Figure 4

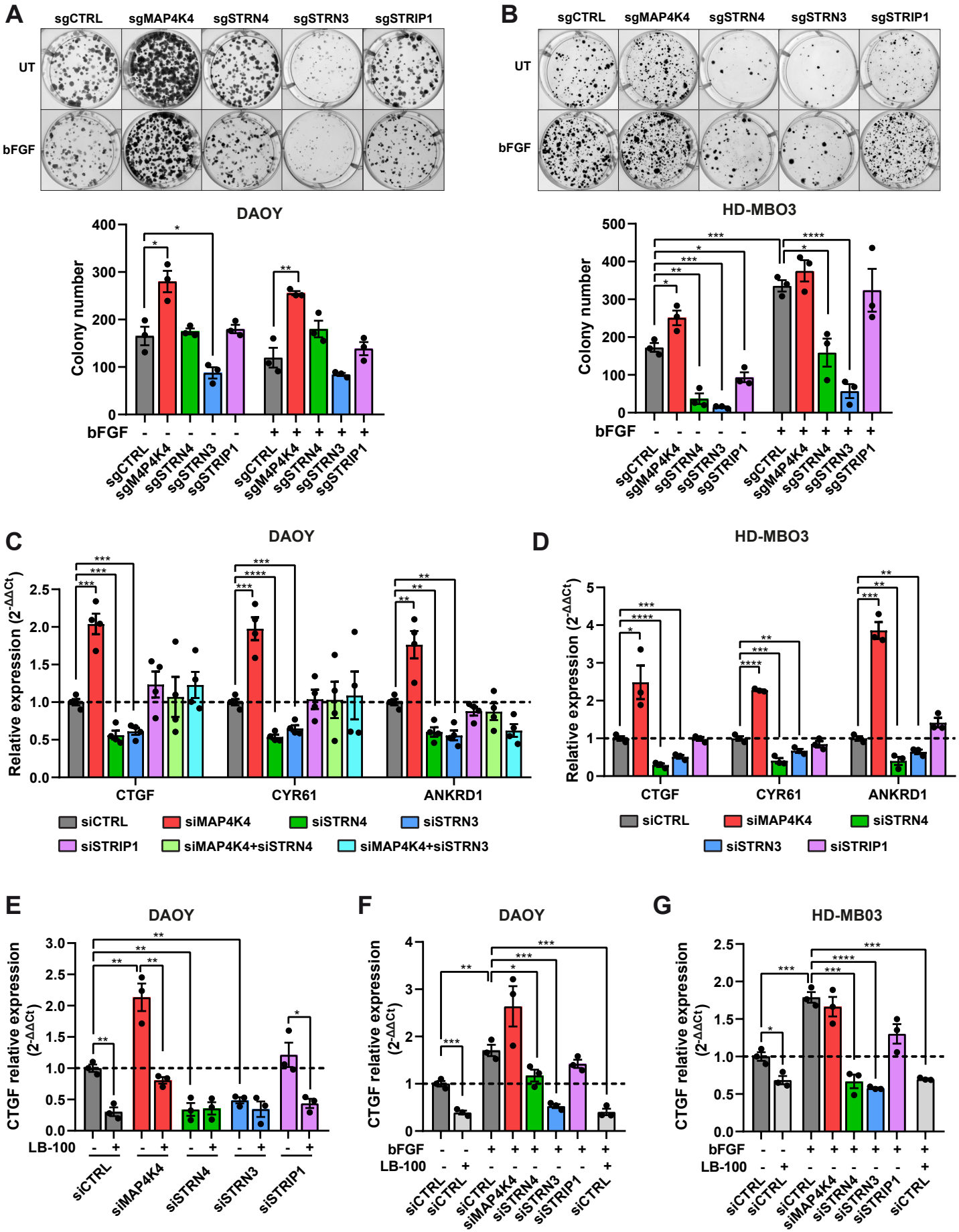
A
sgCTRL
sgMAP4K4
sgSTRN4
sgSTRN3
sgSTRIP1
UT
bFGF
B
DAOY
HD-MBO3
Colony number
bFGF
C
D
Relative expression (2-ΔΔCt)
CTGF
CYR61
ANKRD1
siCTRL
siMAP4K4
siSTRN4
siSTRN3
siSTRIP1
siMAP4K4+siSTRN4
siMAP4K4+siSTRN3
E
F
G
CTGF relative expression (2-ΔΔCt)
LB-100
HD-MB03

Figure 5

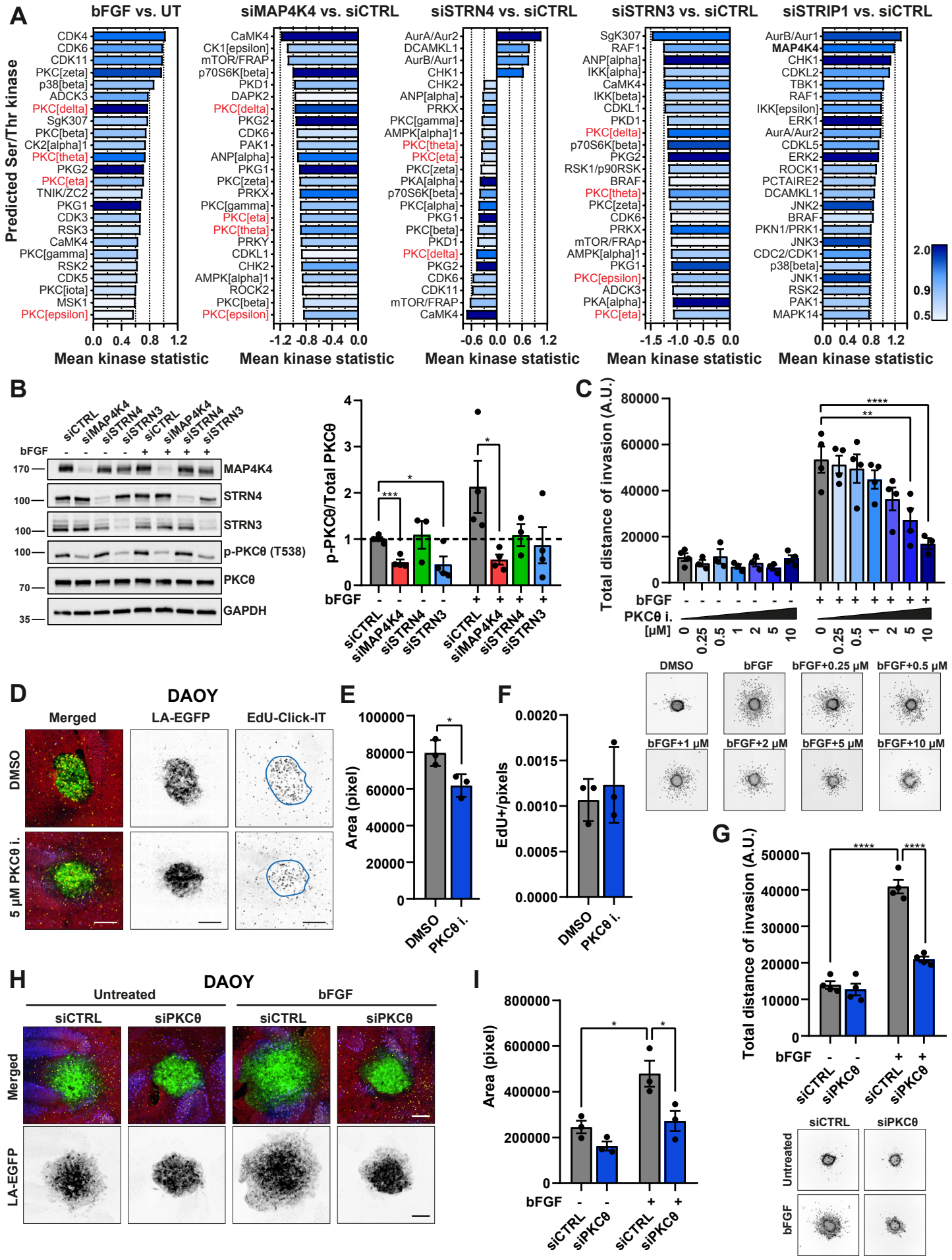
A
bFGF vs. UT
siMAP4K4 vs. siCTRL
siSTRN4 vs. siCTRL
siSTRN3 vs. siCTRL
siSTRIP1 vs. siCTRL
Predicted Ser/Thr kinase
Mean kinase statistic
B
siCTRL
siMAP4K4
siSTRN4
siSTRN3
bFGF
MAP4K4
STRN4
STRN3
p-PKCθ (T538)
PKCθ
GAPDH
p-PKCθ/Total PKCθ
C
Total distance of invasion (A.U.)
PKCθ i.
[μM]
DMSO
bFGF
bFGF+0.25 μM
bFGF+0.5 μM
bFGF+1 μM
bFGF+2 μM
bFGF+5 μM
bFGF+10 μM
D
DAOY
Merged
LA-EGFP
EdU-Click-IT
5 μM PKCθ i.
E
Area (pixel)
F
EdU+/pixels
G
H
Untreated
siPKCθ
I

Figure 6

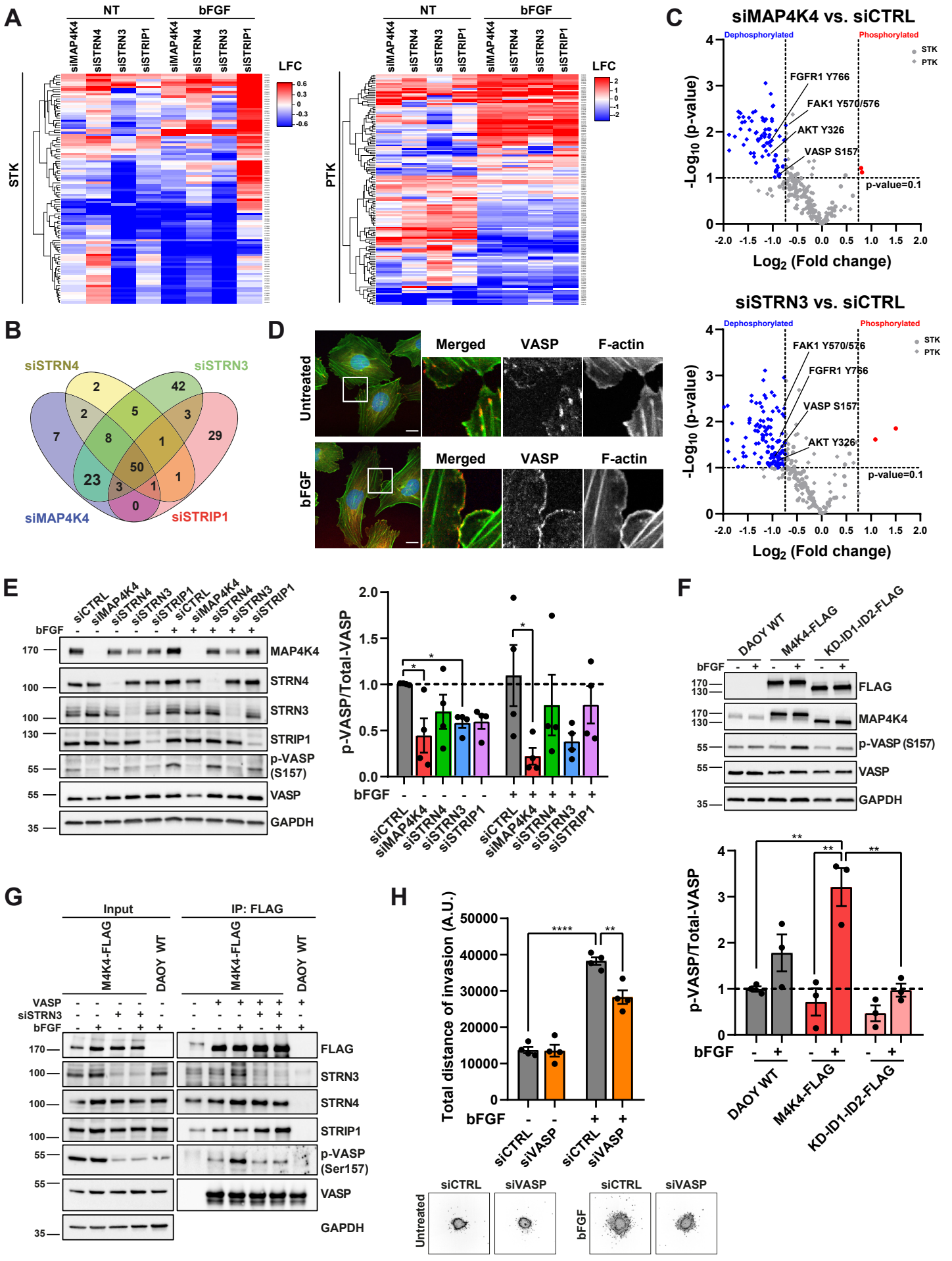
A
NT
bFGF
siMAP4K4
siSTRN4
siSTRN3
siSTRIP1
LFC
STK
PTK
B
siSTRN4
siSTRN3
siMAP4K4
siSTRIP1
C
siMAP4K4 vs. siCTRL
Dephosphorylated
Phosphorylated
STK
PTK
FGFR1 Y766
FAK1 Y570/576
AKT Y326
VASP S157
p-value=0.1
-Log10 (p-value)
Log2 (Fold change)
siSTRN3 vs. siCTRL
D
Untreated
bFGF
Merged
VASP
F-actin
E
siCTRL
siMAP4K4
siSTRN4
siSTRN3
siSTRIP1
bFGF
MAP4K4
STRN4
STRN3
STRIP1
p-VASP (S157)
VASP
GAPDH
p-VASP/Total-VASP
F
DAOY WT
M4K4-FLAG
KD-ID1-ID2-FLAG
FLAG
MAP4K4
p-VASP (S157)
VASP
GAPDH
G
Input
IP: FLAG
M4K4-FLAG
DAOY WT
VASP
siSTRN3
bFGF
FLAG
STRN3
STRN4
STRIP1
p-VASP (Ser157)
VASP
GAPDH
H
Total distance of invasion (A.U.)
bFGF
siCTRL
siVASP
Untreated
bFGF

Figure 7

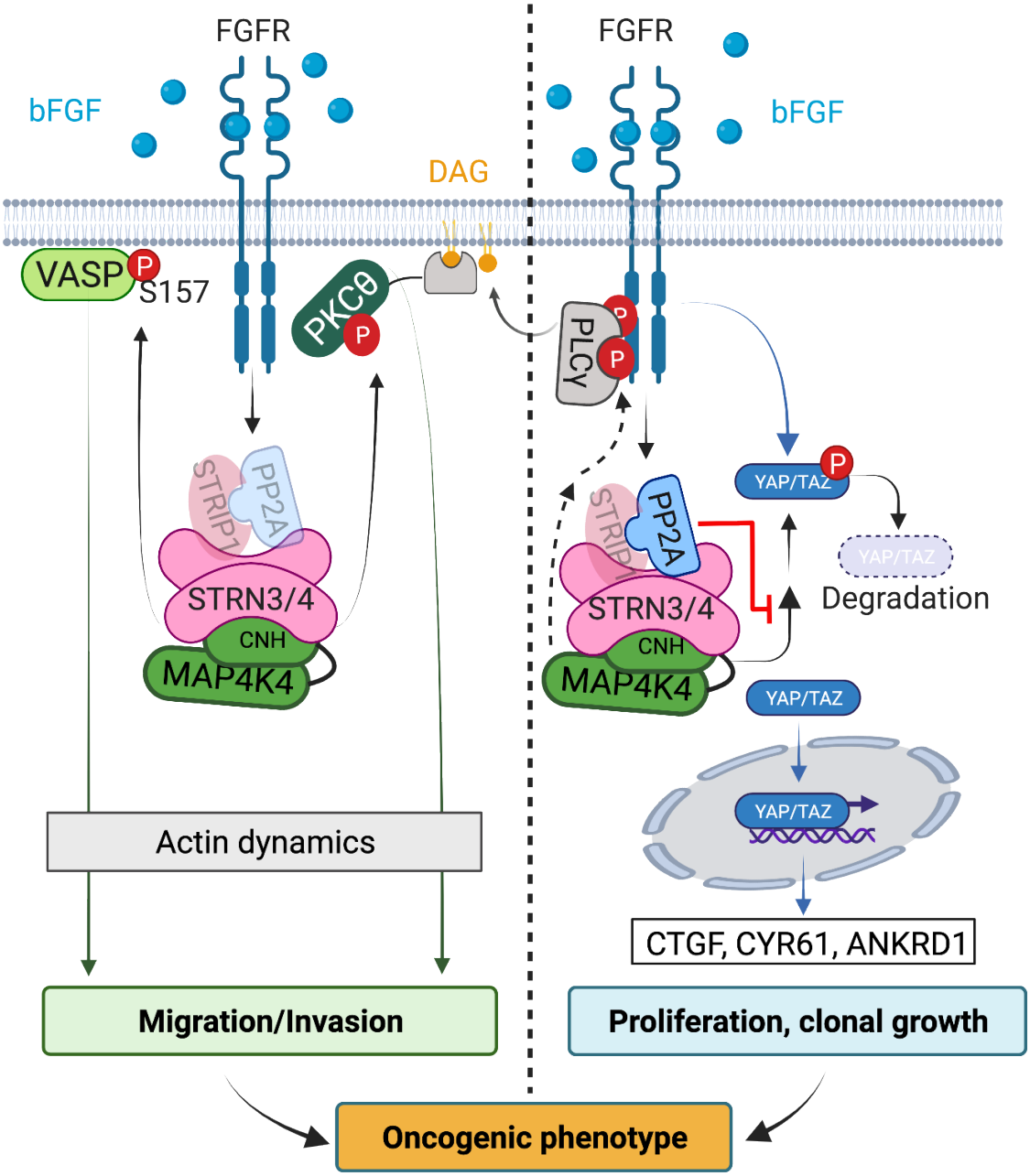
FGFR
bFGF
DAG
VASP
P
S157
PKCθ
P
STRIP1
PP2A
STRN3/4
CNH
MAP4K4
Actin dynamics
Migration/Invasion
FGFR
bFGF
PLCγ
P
P
YAP/TAZ
P
YAP/TAZ
Degradation
STRIP1
PP2A
STRN3/4
CNH
MAP4K4
YAP/TAZ
YAP/TAZ
CTGF, CYR61, ANKRD1
Proliferation, clonal growth
Oncogenic phenotype

Figure S1

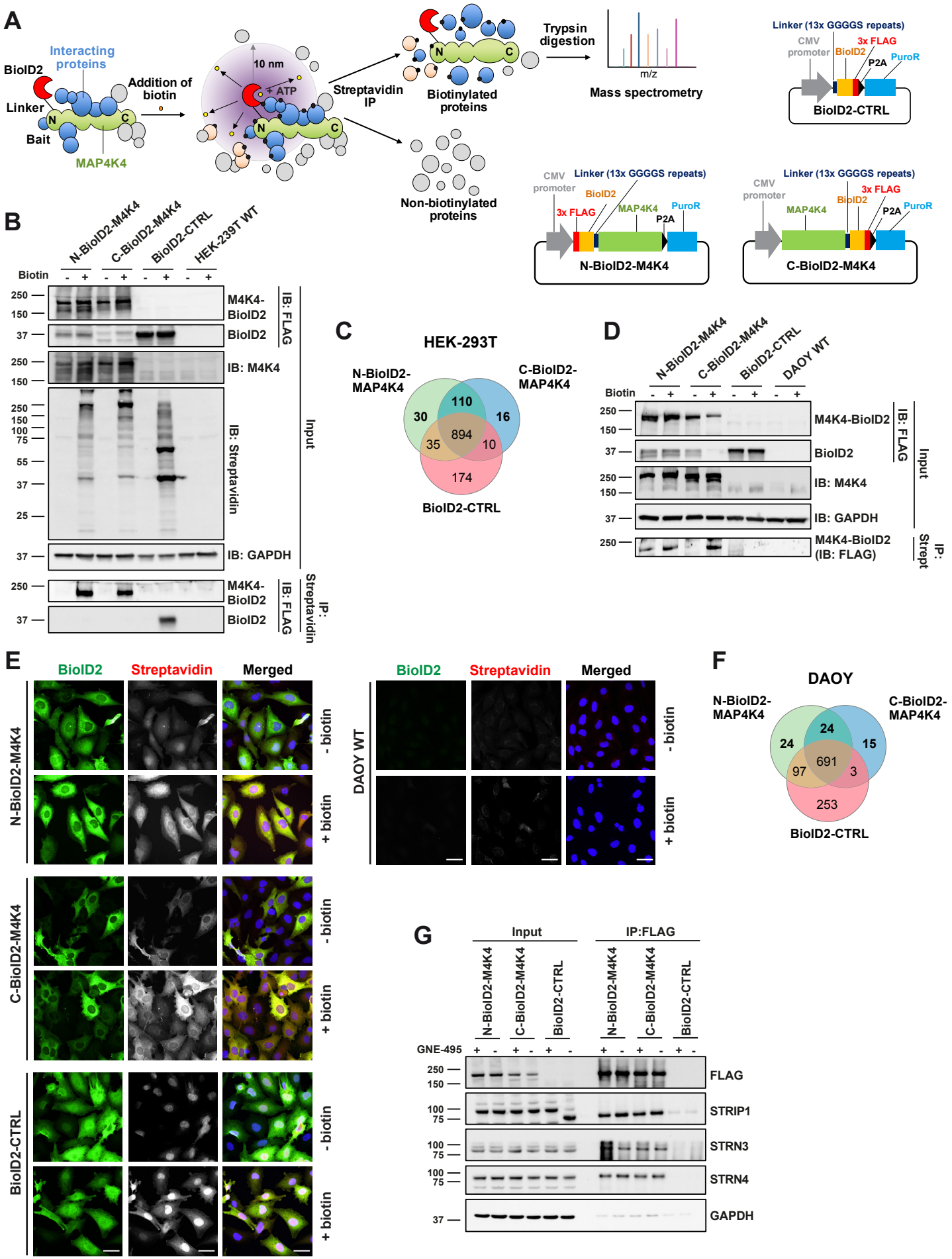
A
Interacting proteins
BioID2
Linker
Bait
MAP4K4
Addition of biotin
10 nm
+ ATP
Streptavidin IP
Biotinylated proteins
Non-biotinylated proteins
Trypsin digestion
m/z
Mass spectrometry
Linker (13x GGGGS repeats)
CMV promoter
3x FLAG
BioID2
P2A
PuroR
BioID2-CTRL
N-BioID2-M4K4
C-BioID2-M4K4
B
N-BioID2-M4K4
C-BioID2-M4K4
BioID2-CTRL
HEK-239T WT
Biotin
M4K4-BioID2
BioID2
IB: FLAG
IB: M4K4
IB: Streptavidin
IB: GAPDH
Input
IP: Streptavidin
C
HEK-293T
N-BioID2-MAP4K4
C-BioID2-MAP4K4
BioID2-CTRL
110
30
16
894
35
10
174
D
N-BioID2-M4K4
C-BioID2-M4K4
BioID2-CTRL
DAOY WT
Biotin
M4K4-BioID2
BioID2
IB: M4K4
IB: GAPDH
M4K4-BioID2 (IB: FLAG)
IP: Strept
E
BioID2
Streptavidin
Merged
N-BioID2-M4K4
C-BioID2-M4K4
BioID2-CTRL
DAOY WT
- biotin
+ biotin
F
DAOY
N-BioID2-MAP4K4
C-BioID2-MAP4K4
BioID2-CTRL
24
24
15
691
97
3
253
G
Input
IP:FLAG
N-BioID2-M4K4
C-BioID2-M4K4
BioID2-CTRL
GNE-495
FLAG
STRIP1
STRN3
STRN4
GAPDH

Figure S2

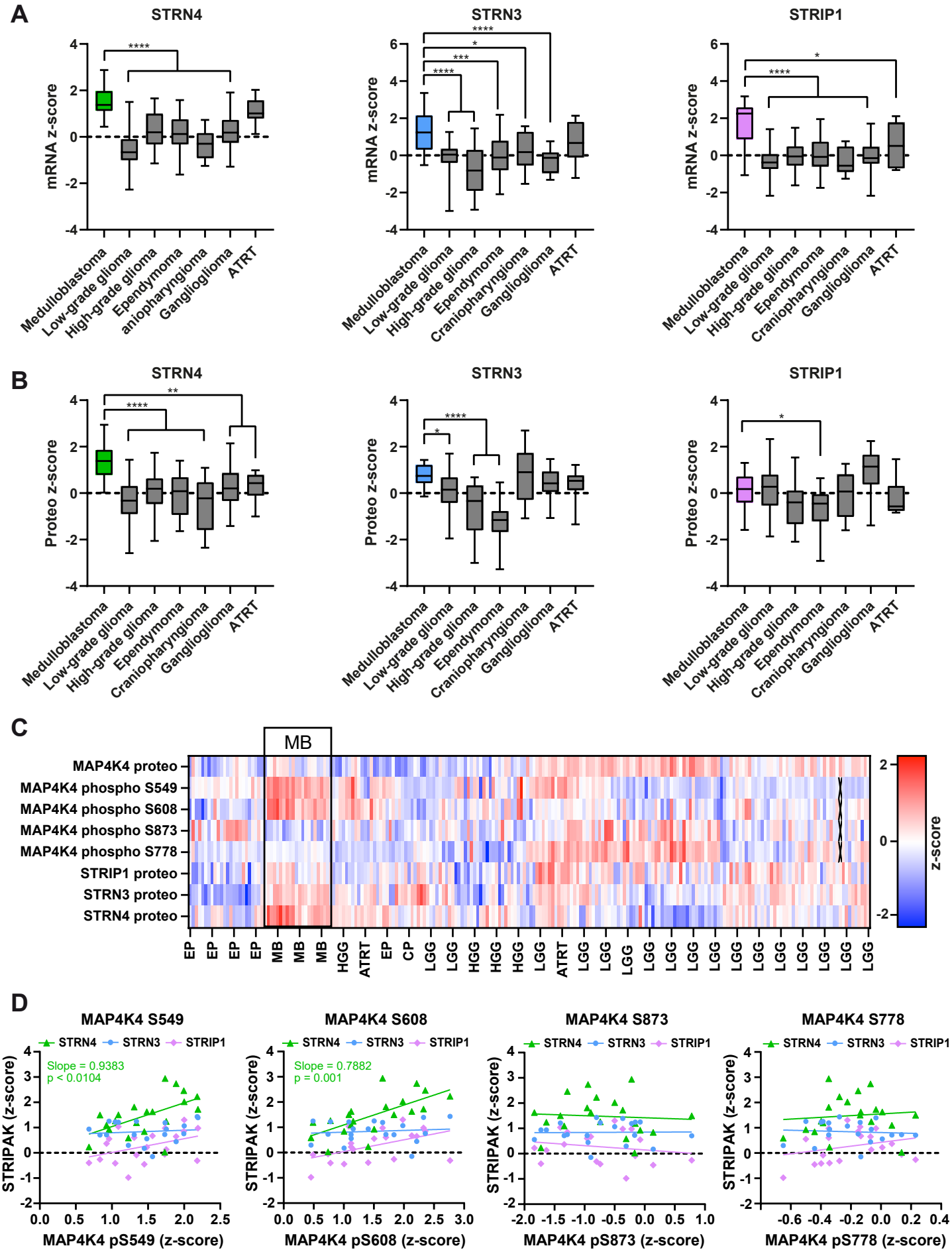
A
STRN4
STRN3
STRIP1
mRNA z-score
Medulloblastoma
Low-grade glioma
High-grade glioma
Ependymoma
aniopharyngioma
Craniopharyngioma
Ganglioglioma
ATRT
B
Proteo z-score
C
MB
MAP4K4 proteo
MAP4K4 phospho S549
MAP4K4 phospho S608
MAP4K4 phospho S873
MAP4K4 phospho S778
STRIP1 proteo
STRN3 proteo
STRN4 proteo
z-score
EP
CP
HGG
LGG
D
MAP4K4 S549
MAP4K4 S608
MAP4K4 S873
MAP4K4 S778
STRN4
STRN3
STRIP1
Slope = 0.9383
p < 0.0104
Slope = 0.7882
p = 0.001
STRIPAK (z-score)
MAP4K4 pS549 (z-score)
MAP4K4 pS608 (z-score)
MAP4K4 pS873 (z-score)
MAP4K4 pS778 (z-score)

Figure S3

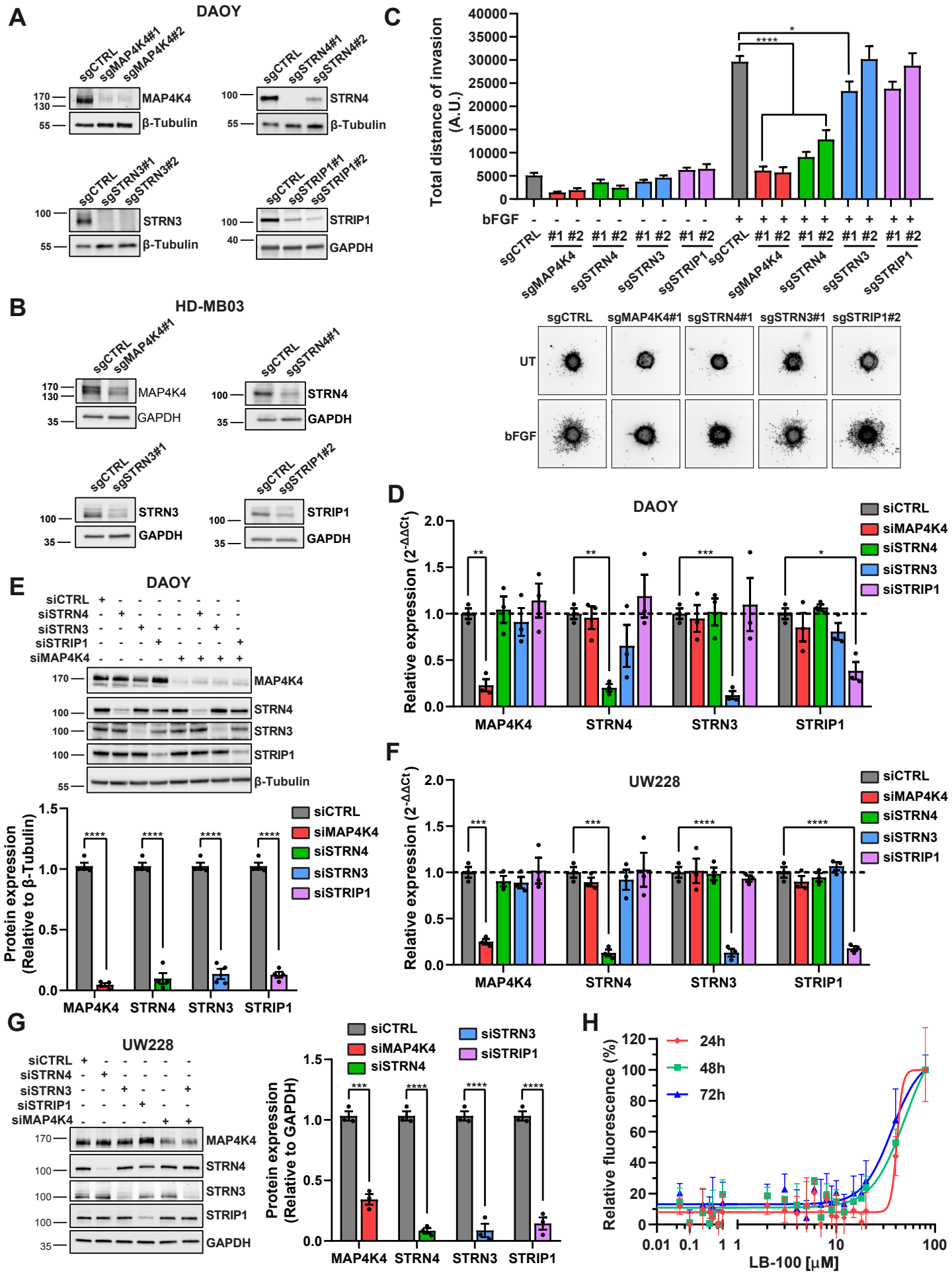
A
DAOY
sgCTRL
sgMAP4K4#1
sgMAP4K4#2
MAP4K4
β-Tubulin
sgSTRN4#1
sgSTRN4#2
STRN4
sgSTRN3#1
sgSTRN3#2
STRN3
sgSTRIP1#1
sgSTRIP1#2
STRIP1
GAPDH
B
HD-MB03
C
Total distance of invasion (A.U.)
bFGF
UT
D
DAOY
Relative expression ($2^{-\Delta\Delta Ct}$)
siCTRL
siMAP4K4
siSTRN4
siSTRN3
siSTRIP1
E
Protein expression (Relative to β-Tubulin)
F
UW228
G
Protein expression (Relative to GAPDH)
H
Relative fluorescence (%)
24h
48h
72h
LB-100 [μM]

Figure S4

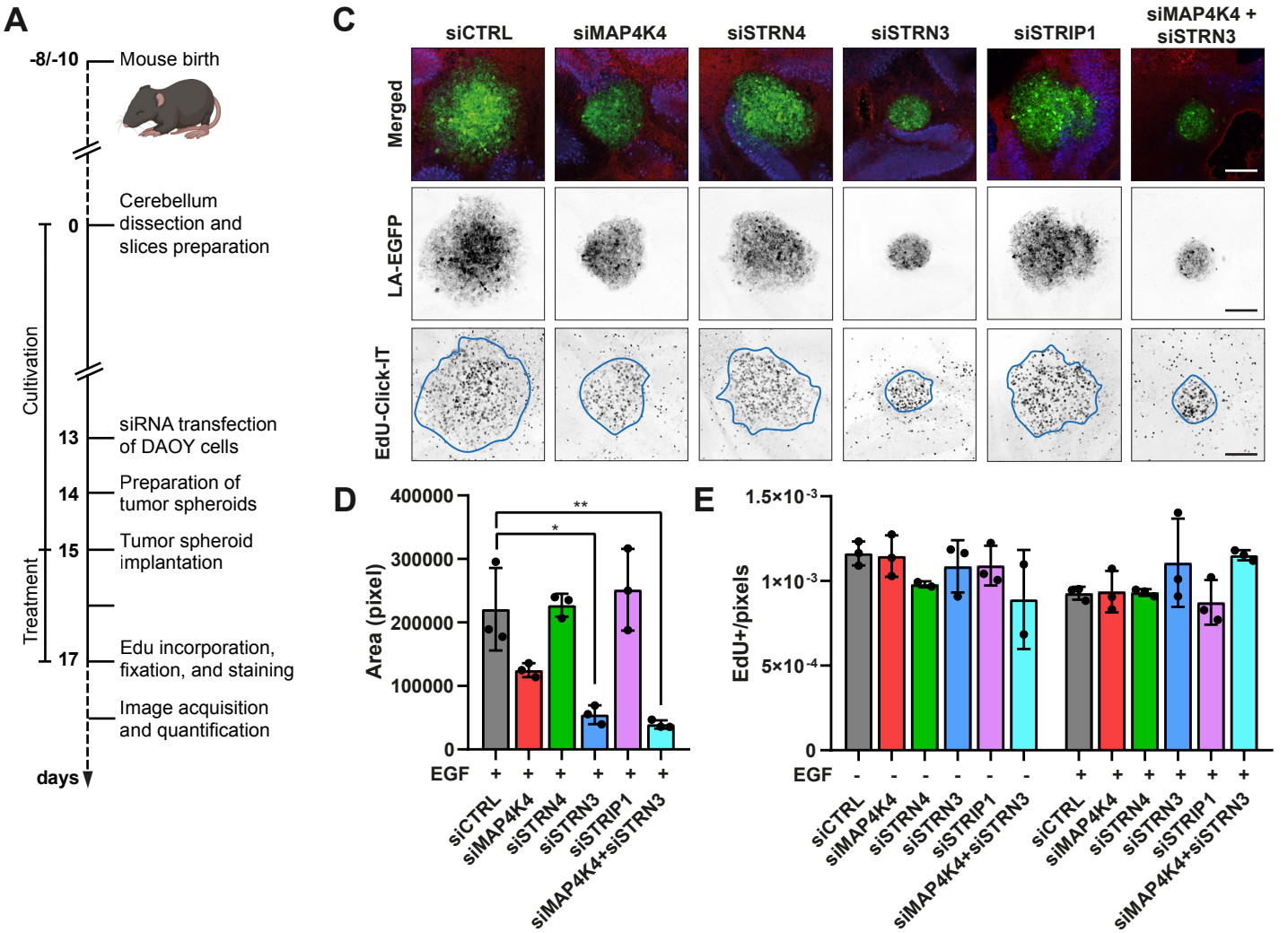
A
-8/-10
Mouse birth
Cerebellum dissection and slices preparation
0
Cultivation
13
siRNA transfection of DAOY cells
14
Preparation of tumor spheroids
15
Tumor spheroid implantation
Treatment
17
Edu incorporation, fixation, and staining
Image acquisition and quantification
days
C
siCTRL
siMAP4K4
siSTRN4
siSTRN3
siSTRIP1
siMAP4K4 + siSTRN3
Merged
LA-EGFP
EdU-Click-IT
D
Area (pixel)
400000
300000
200000
100000
0
**
*
EGF
siCTRL
siMAP4K4
siSTRN4
siSTRN3
siSTRIP1
siMAP4K4+siSTRN3
E
EdU+/pixels
1.5×10-3
1×10-3
5×10-4
0
EGF

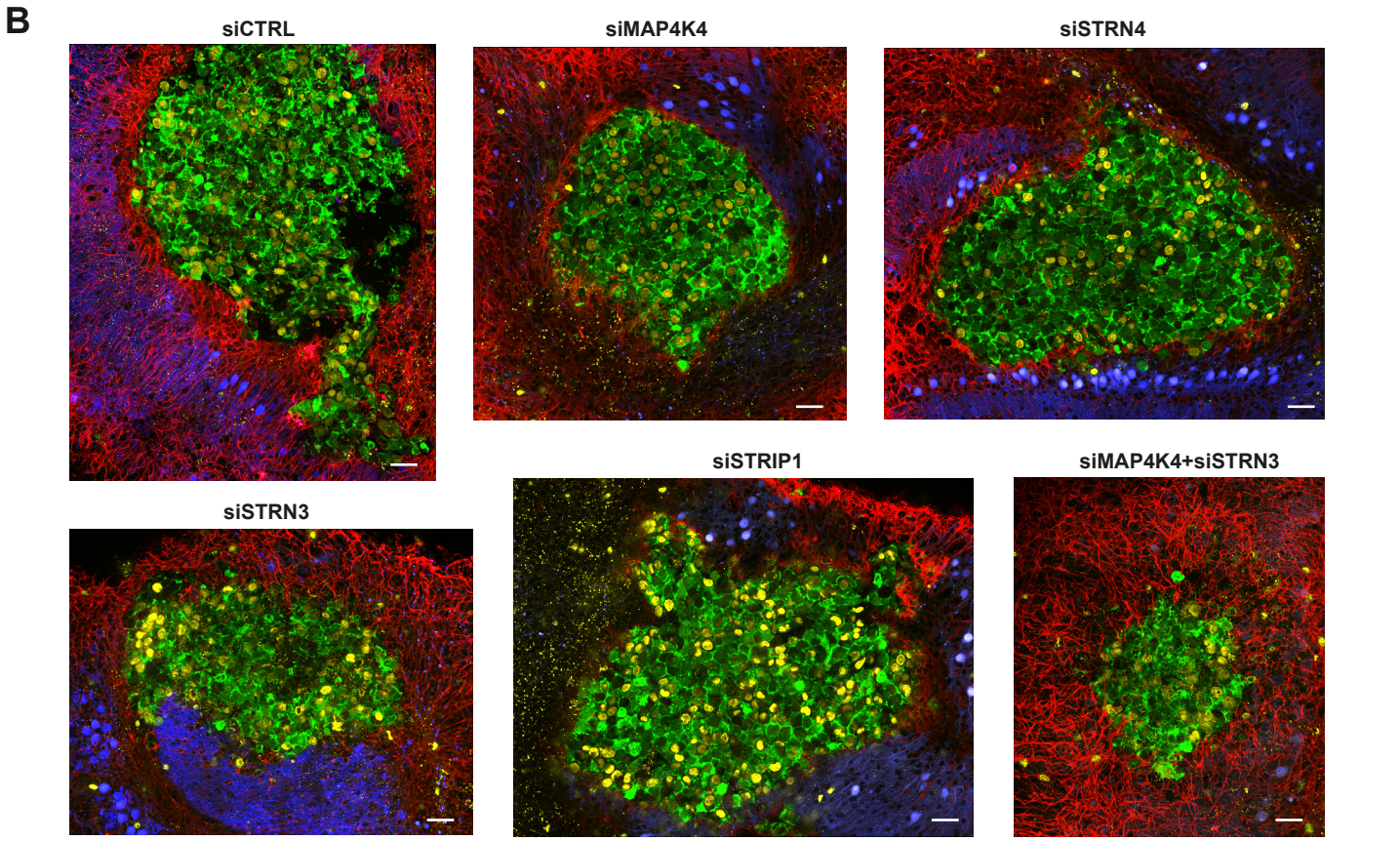
B
siCTRL
siMAP4K4
siSTRN4
siSTRN3
siSTRIP1
siMAP4K4+siSTRN3

Figure S5

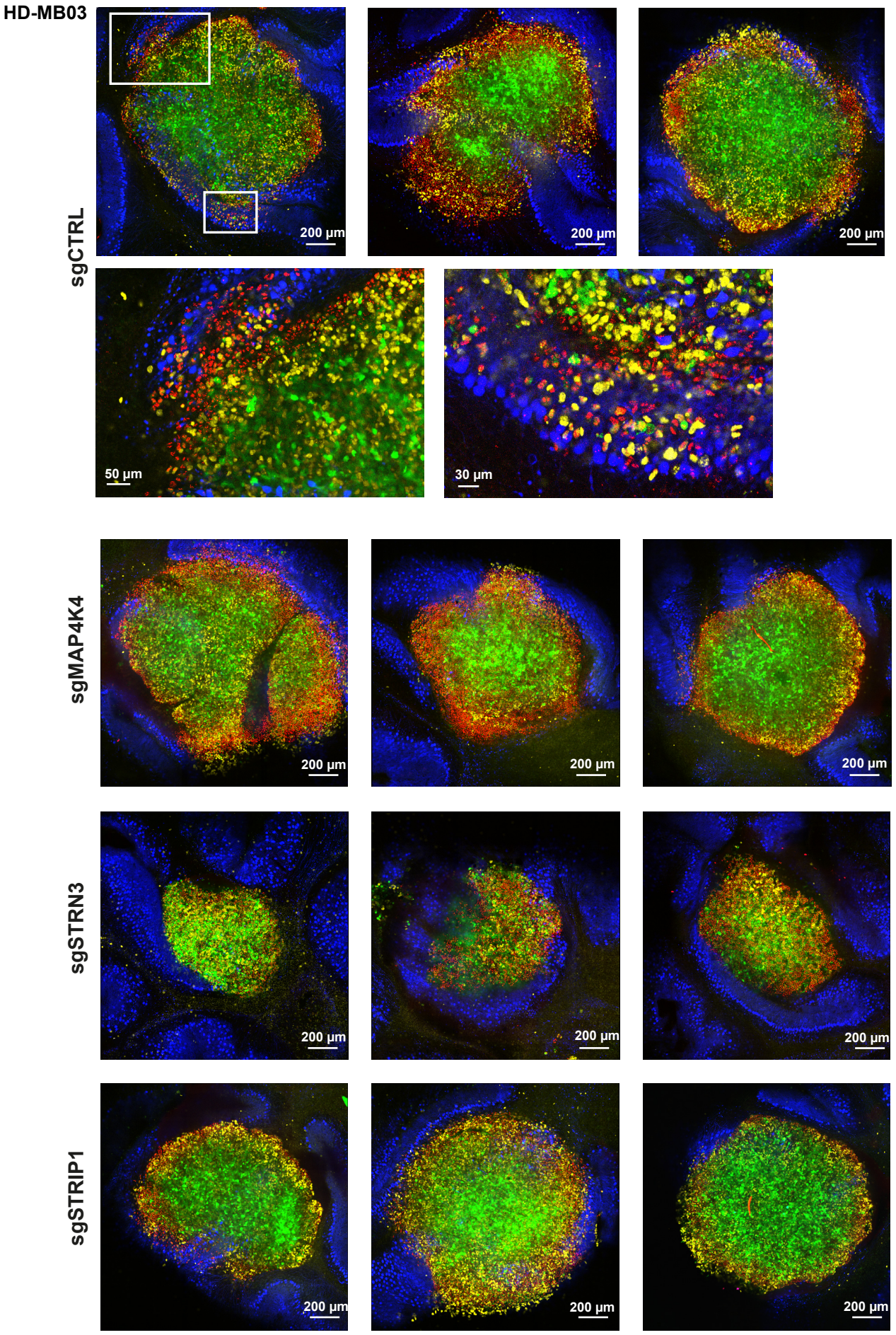

Figure S6

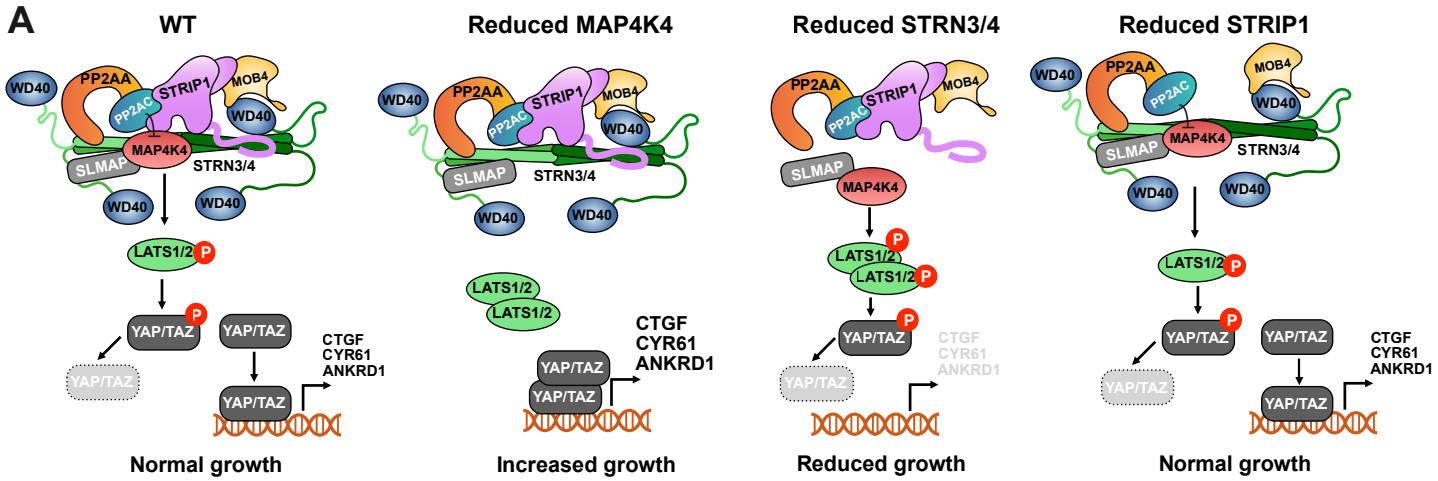
A
WT
Reduced MAP4K4
Reduced STRN3/4
Reduced STRIP1
WD40
PP2AA
PP2AC
STRIP1
MOB4
SLMAP
MAP4K4
STRN3/4
LATS1/2
P
YAP/TAZ
CTGF
CYR61
ANKRD1
Normal growth
Increased growth
Reduced growth
Normal growth

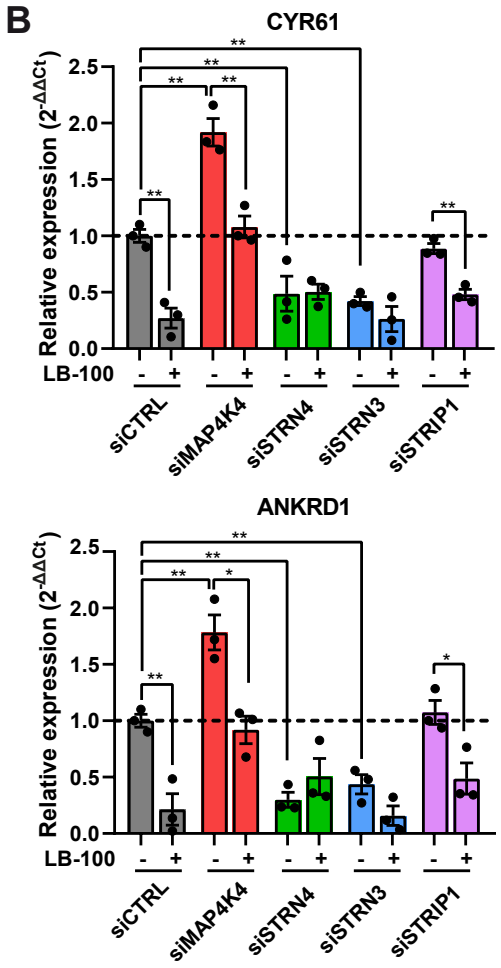
B
CYR61
ANKRD1
Relative expression (2^-ΔΔCt)
LB-100
siCTRL
siMAP4K4
siSTRN4
siSTRN3
siSTRIP1

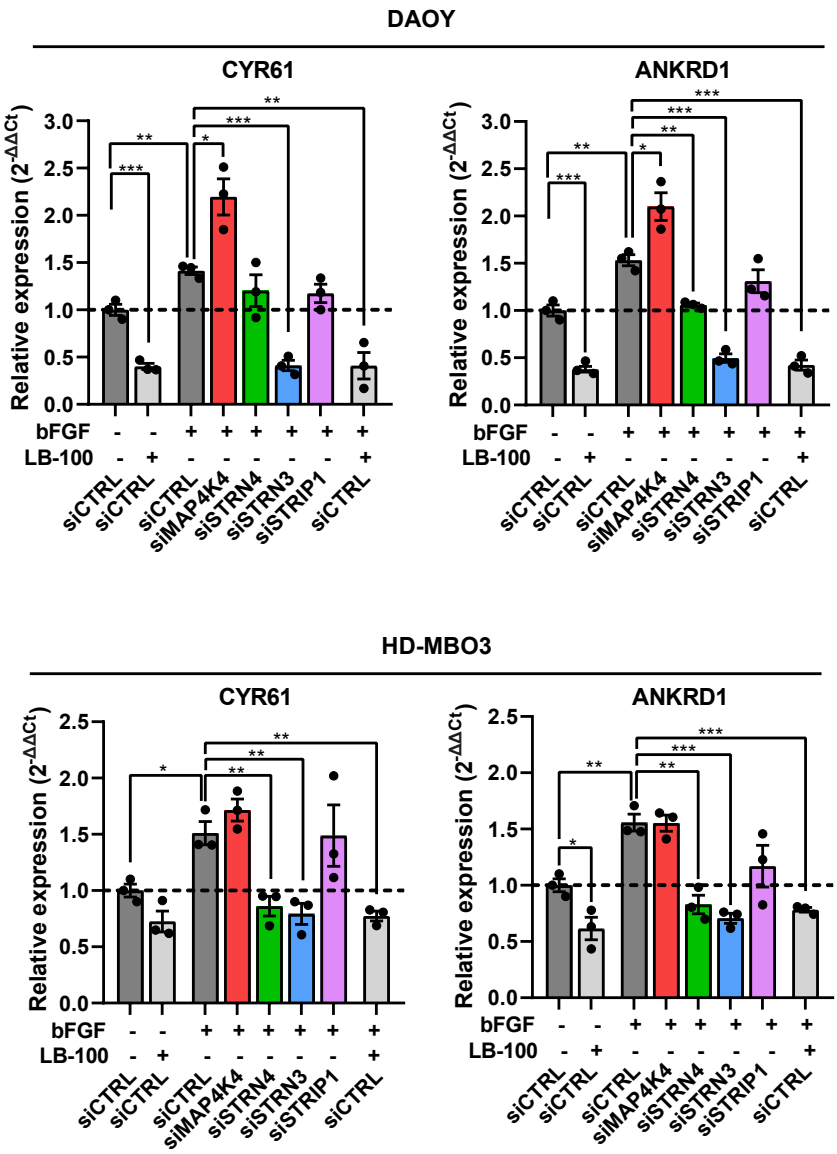
C
DAOY
CYR61
ANKRD1
D
HD-MBO3
Relative expression (2^-ΔΔCt)
bFGF
LB-100
siCTRL
siMAP4K4
siSTRN4
siSTRN3
siSTRIP1

Figure S7

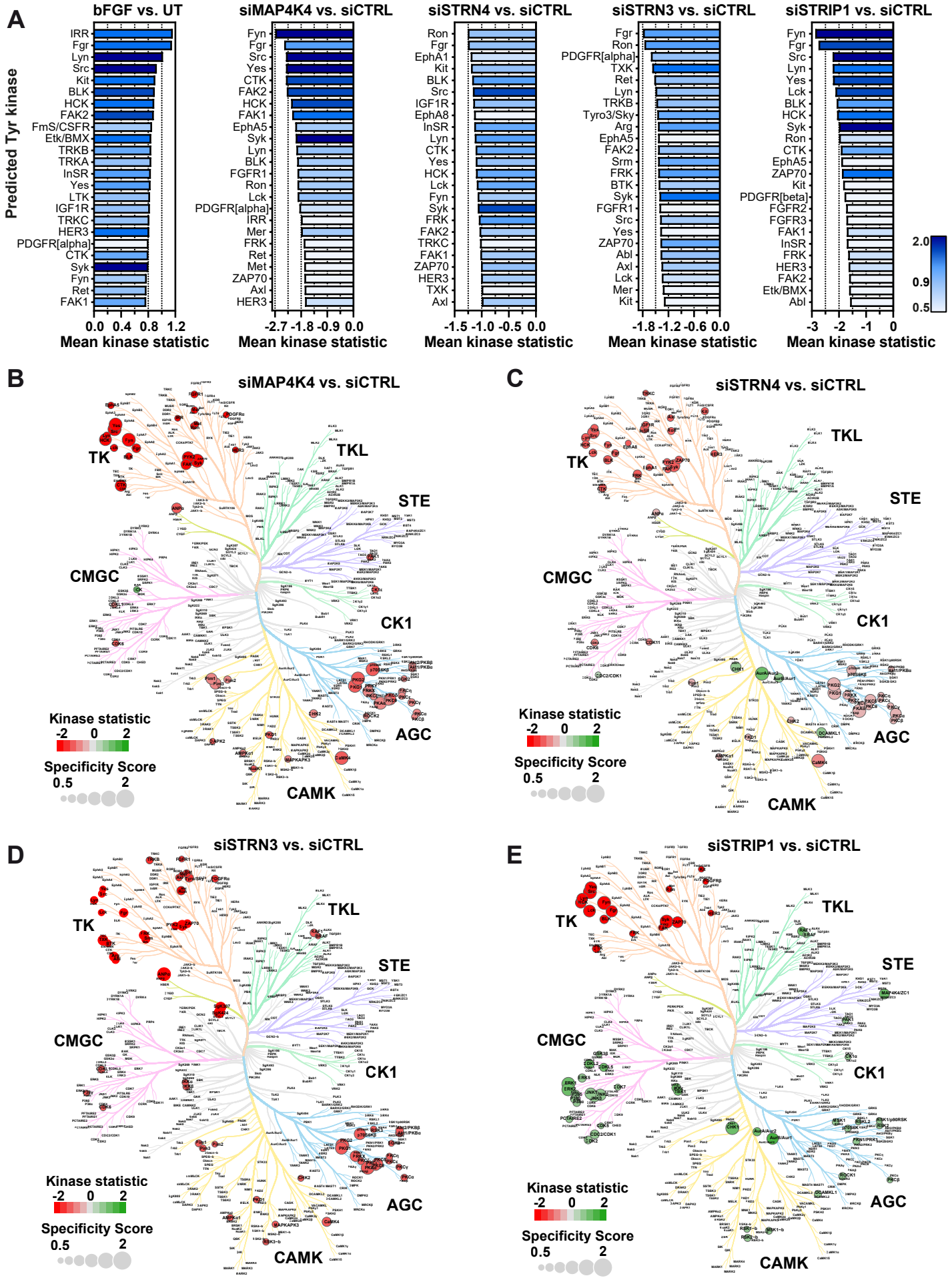
A
bFGF vs. UT
siMAP4K4 vs. siCTRL
siSTRN4 vs. siCTRL
siSTRN3 vs. siCTRL
siSTRIP1 vs. siCTRL
Predicted Tyr kinase
Mean kinase statistic
B
siMAP4K4 vs. siCTRL
C
siSTRN4 vs. siCTRL
D
siSTRN3 vs. siCTRL
E
siSTRIP1 vs. siCTRL
TK
TKL
STE
CMGC
CK1
AGC
CAMK
Kinase statistic
-2 0 2
Specificity Score
0.5 2

Figure S8

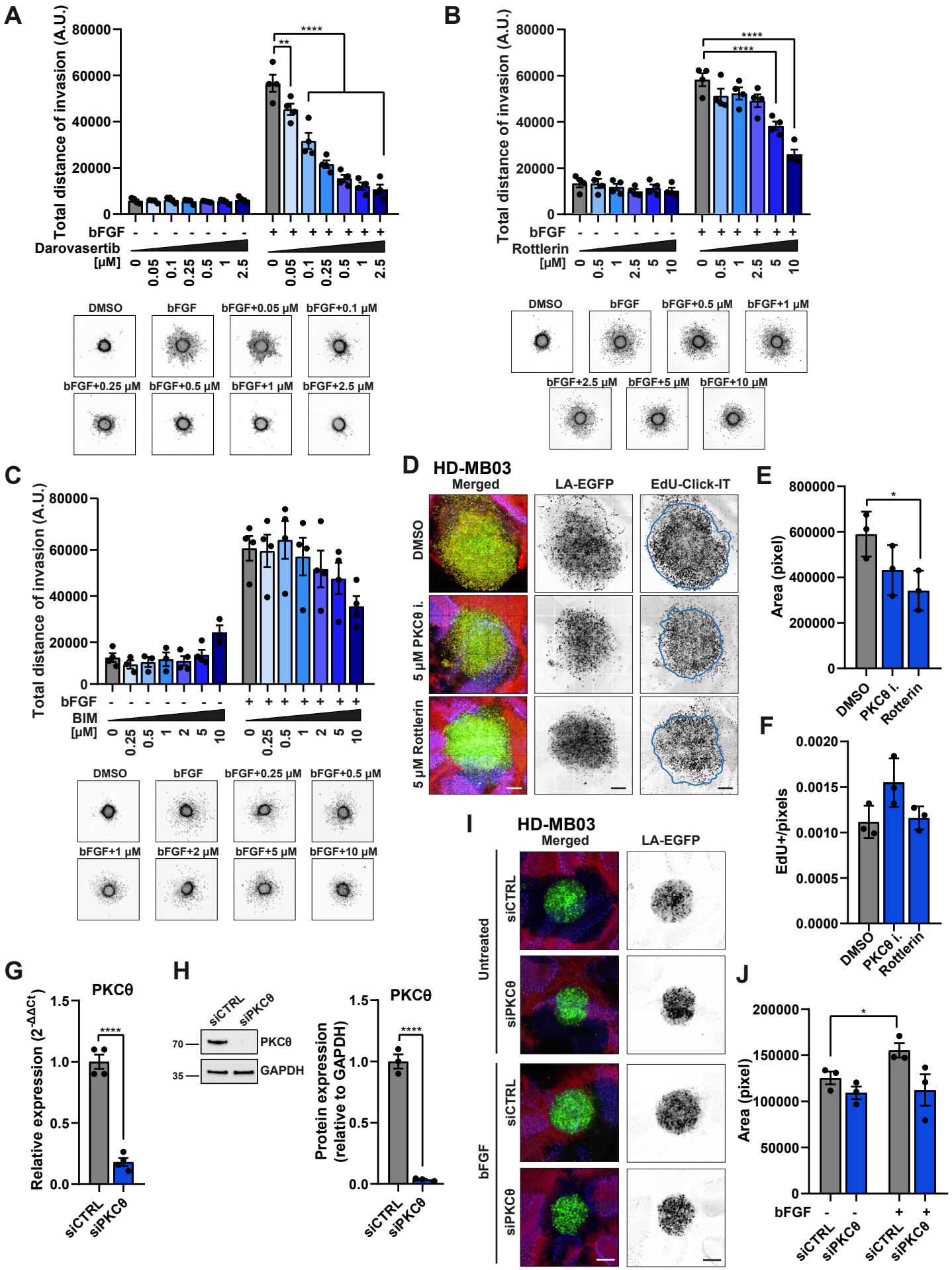
A
Total distance of invasion (A.U.)
80000
60000
40000
20000
0
bFGF
Darovasertib [μM]
0 0.05 0.1 0.25 0.5 1 2.5
DMSO
bFGF
bFGF+0.05 μM
bFGF+0.1 μM
bFGF+0.25 μM
bFGF+0.5 μM
bFGF+1 μM
bFGF+2.5 μM
B
Rottlerin [μM]
0 0.5 1 2.5 5 10
bFGF+0.5 μM
bFGF+1 μM
bFGF+2.5 μM
bFGF+5 μM
bFGF+10 μM
C
BIM [μM]
0 0.25 0.5 1 2 5 10
bFGF+0.25 μM
bFGF+0.5 μM
bFGF+1 μM
bFGF+2 μM
bFGF+5 μM
bFGF+10 μM
D
HD-MB03
Merged
LA-EGFP
EdU-Click-IT
DMSO
5 μM PKCθ i.
5 μM Rottlerin
E
Area (pixel)
DMSO
PKCθ i.
Rotterin
F
EdU+/pixels
G
PKCθ
Relative expression (2^-ΔΔCt)
siCTRL
siPKCθ
H
70
35
GAPDH
Protein expression (relative to GAPDH)
I
Untreated
bFGF
J

Figure S9

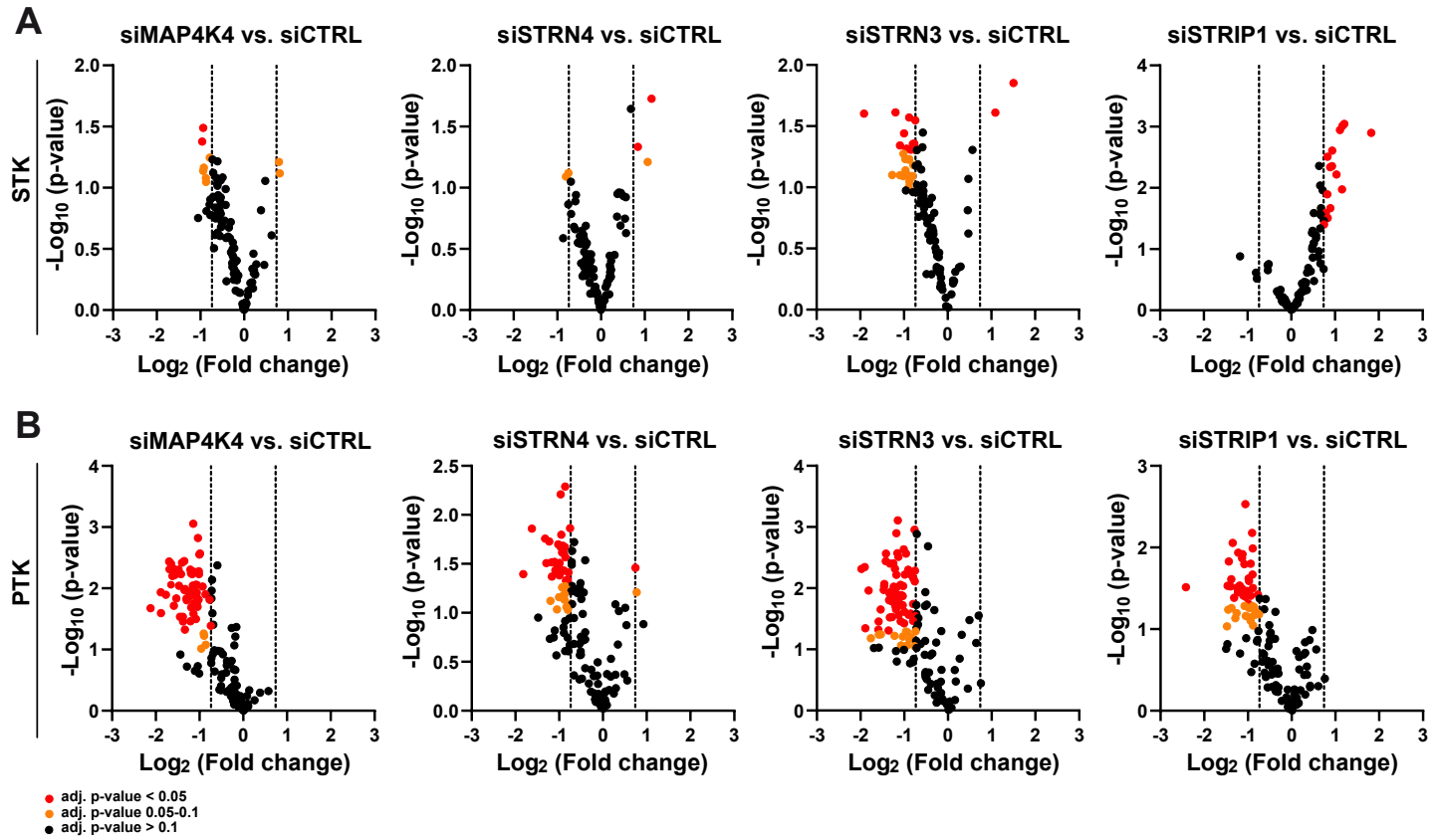
A
siMAP4K4 vs. siCTRL
siSTRN4 vs. siCTRL
siSTRN3 vs. siCTRL
siSTRIP1 vs. siCTRL
STK
-Log10 (p-value)
Log2 (Fold change)
B
siMAP4K4 vs. siCTRL
siSTRN4 vs. siCTRL
siSTRN3 vs. siCTRL
siSTRIP1 vs. siCTRL
PTK
-Log10 (p-value)
Log2 (Fold change)
adj. p-value < 0.05
adj. p-value 0.05-0.1
adj. p-value > 0.1

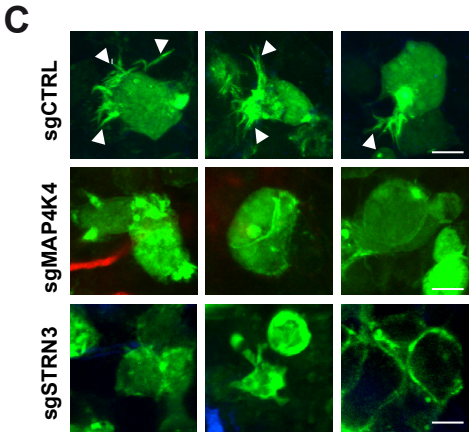
C
sgCTRL
sgMAP4K4
sgSTRN3

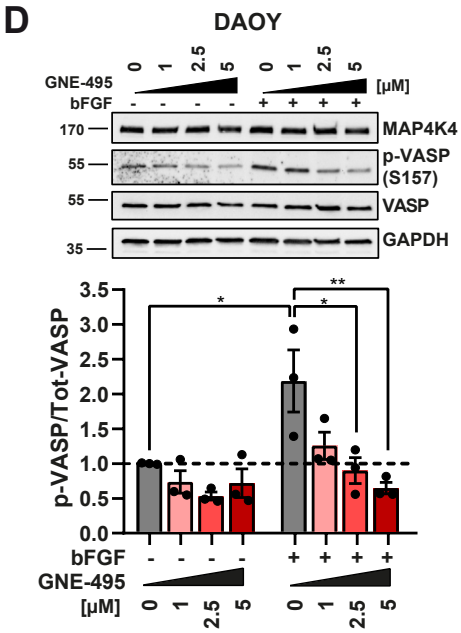
D
DAOY
GNE-495
bFGF
[μM]
MAP4K4
p-VASP (S157)
VASP
GAPDH
p-VASP/Tot-VASP

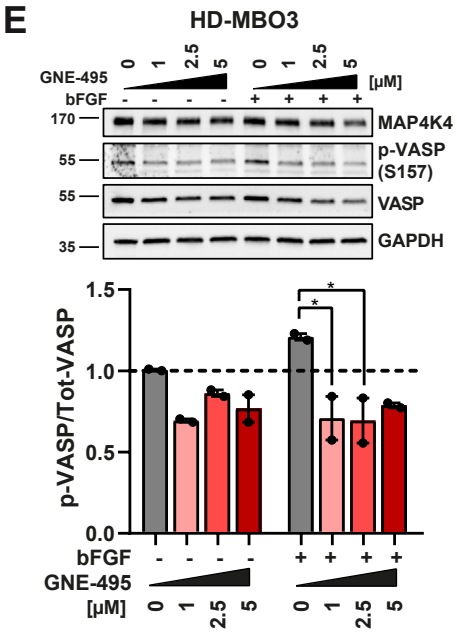
E
HD-MBO3
GNE-495
bFGF
[μM]
MAP4K4
p-VASP (S157)
VASP
GAPDH
p-VASP/Tot-VASP

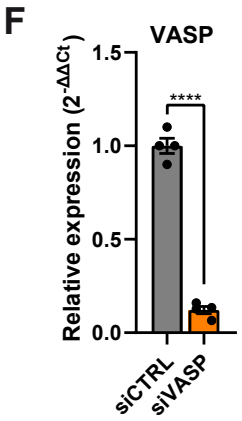
F
VASP
Relative expression (2-ΔΔCt)
siCTRL
siVASP

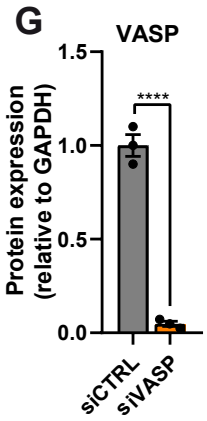
G
VASP
Protein expression (relative to GAPDH)
siCTRL
siVASP

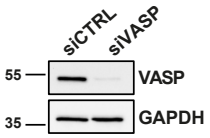
siCTRL
siVASP
VASP
GAPDH